NASA Contractor Report CR-1998-208540

Final Report on Prototype Local Data Integration System and Central Florida Data Deficiency

Prepared By:
Applied Meteorology Unit

Prepared for:
Kennedy Space Center
Under Contract NAS10-96018

NASA
National Aeronautics and
Space Administration

Office of Management

Scientific and Technical
Information Program

1998

Attributes and Acknowledgments

NASA/KSC POC:
Dr. Francis J. Merceret
AA-C-1

Applied Meteorology Unit (AMU)

John Manobianco
Jonathan Case

Table of Contents

List of Figures

List of Tables

List of Acronyms

Term	Description
45 WS	45th Weather Squadron
ACARS	ARINC Communications, Addressing and Reporting System
ACE	Army Corps of Engineers
ADAS	ARPS Data Analysis System
AMU	Applied Meteorology Unit
ARINC	Aeronautical Radio, Inc.
ARM	Atmospheric Radiation Measurement
ARPS	Advanced Regional Prediction System
ASOS	Automated Surface Observing System
AWIPS	Automated Weather Interactive Processing System
CAPS	Center for Analysis and Prediction of Storms
CC	Correlation Coefficient
CCAS	Cape Canaveral Air Station
CCS	Complex Cloud Scheme
CSR	Computer Sciences Raytheon
DNI	Data Non-Incorporation
FPDT	Forecast Products Development Team
FSL	Forecast Systems Laboratory
FWMD	Florida Water Management Districts
GOES	Geostationary Orbiting Environmental Satellite
IR	Infrared
ITWS	Integrated Terminal Weather System
KSC	Kennedy Space Center
LAPS	Local Analysis and Prediction System
LDIS	Local Data Integration System
MB	Megabytes
MESO	Mesoscale Environmental Simulations and Operations
METAR	Aviation Routine Weather Report
MIDDS	Meteorological Interactive Data Display System
MLB	Melbourne, FL
NCDC	National Climatic Data Center
NDBC	National Data Buoy Center
NESDIS	National Environmental Satellite Data and Information Service
NEXRAD	Next Generation Radar

NIDS	NEXRAD Information Dissemination Service
NOAA	National Oceanic and Atmospheric Administration
NWS	National Weather Service
OI	Optimum Interpolation
ORA	Office of Research Applications
PIREPS	Pilot Reports
POC	Point of Contact
QC	Quality Control
RH	Relative Humidity
RUC	Rapid Update Cycle
SCM	Successive Corrections Method
SHEF	Standardized Hydrologic Exchange Format
SMG	Space Meteorology Group
SSEC	Space Science and Engineering Center
SST	Sea-Surface Temperature
TPA	Tampa, FL
USGS	United States Geological Survey
WSR-88D	Weather Surveillance Radar-1988 Doppler
WV	Water Vapor

Executive Summary

This report describes the Applied Meteorology Unit's (AMU) task on the Local Data Integration System (LDIS) and central Florida data deficiency. The objectives of the task are to identify all existing meteorological data sources within 250 km of the Kennedy Space Center (KSC) and the Eastern Range at Cape Canaveral Air Station (CCAS), identify and configure an appropriate LDIS to integrate these data, and implement a working prototype to be used for limited case studies and data non-incorporation (DNI) experiments.

The ultimate goal for running LDIS is to generate products that may enhance weather nowcasts and short-range (< 6 h) forecasts issued in support of the 45th Weather Squadron (45 WS), Spaceflight Meteorology Group (SMG), and the Melbourne National Weather Service (NWS MLB) operational requirements. The LDIS has the potential to provide added value for nowcasts and short term forecasts for two reasons. First, it incorporates all data operationally available in east central Florida. Second, it is run at finer spatial and temporal resolutions than current national-scale operational models. In combination with a suitable visualization tool, LDIS may provide users with a more complete and comprehensive understanding of evolving fine-scale weather features than could be developed by individually examining the disparate data sets over the same area and time.

The utility of LDIS depends largely on the reliability and availability of observational data. Therefore, it is important to document all existing meteorological data sources around central Florida that can be incorporated by it. Several factors contribute to the data density and coverage over east central Florida including the level in the atmosphere, distance from KSC/CCAS, time, and prevailing weather. The central Florida mesonet consists of existing surface meteorological and hydrological data available from the Tampa NWS and data servers at Miami and Jacksonville. However the utility of these data for operational use is limited, mainly because there are relatively few additional meteorological observations within 50 km of KSC/CCAS to supplement existing METAR and KSC/CCAS tower reports.

The LDIS software of choice is the Advanced Regional Prediction System (ARPS) Data Analysis System (ADAS). ADAS was configured to generate high-resolution analyses in space and time for a warm (26-27 July 1997) and cool season case (12 December 1997). Wind and cloud results are presented for both case studies in order to demonstrate the fidelity and utility of LDIS. DNI experiments are conducted in order to illustrate the impact of missing data on ADAS analyses.

Fidelity is defined as the reliability of LDIS in generating features that are observed in the disparate data sets. It is important to examine fidelity in order to ensure that LDIS is capable of capturing these features when integrating many different data sources. The trends in the ADAS analyses display a good fit to the observed trends with the exception of a few significant differences. An exact representation of specific observations is not anticipated because ADAS incorporates observational and background errors, computes grid values based on nearby observations, and integrates many different types of data.

The utility of the LDIS is given by the value or usefulness that it can provide by integrating disparate data sets to generate analysis products that are not typically available to weather forecasters. The following points highlight the specific added value of LDIS as determined in this study:

- High-resolution analyses can depict the formation and propagation of a thunderstorm outflow boundary. The detailed structure of winds associated with the outflow boundary in the warm season case is much easier to visualize using ADAS rather than Weather Surveillance Radar-1988 Doppler (WSR-88D) radial velocity data.

- Cross sections of primary and diagnostic quantities can be used to examine fine-scale spatial and temporal structures of thunderstorms that are not resolved by current national-scale operational models.

- The Complex Cloud Scheme (CCS) of ADAS derives products such as cloud ceiling, cloud tops, fractional cloud coverage, etc. at very high temporal and spatial resolutions. These high-resolution products are accurate depictions of satellite cloud fields and cannot be easily obtained from the individual data sets.

- The ability to simultaneously display cloud liquid water, cloud ice, rain water, and temperature analyses can provide forecasters with information to help diagnose cloud thickness, cloud heights, ceilings, and possible cloud electrification.

The DNI results show that WSR-88D data have the greatest impact on the wind and moisture analyses for both the warm and cool season events. The influence of WSR-88D data can be misleading in these results since both case studies are characterized by widespread precipitation and thus the presence of numerous radar targets. A quiescent weather pattern would probably produce a much smaller impact from WSR-88D data.

An extension to the LDIS task is currently underway to examine issues relating to its operational implementation. For example, examination of output from the prototype configuration of ADAS reveals that its utility may be limited by a lack of temporal continuity between successive analyses. An extension of the current AMU LDIS task will address such issues while modifying the configuration in order to simulate a real-time LDIS.

1.0 Introduction

1.1 Task History and Objectives

Prior to the 1996 Applied Meteorology Unit (AMU) Tasking and Prioritization meeting, the Spaceflight Meteorology Group (SMG) proposed a Florida mesonet task. The Florida mesonet task was approved by consensus at the meeting in April 1996. For this task, the AMU was to determine requirements for a central Florida mesonet including recommendations on the domain, site locations, spatial resolution, and instrumentation type. In preparation for the 1997 T&P meeting, SMG resubmitted the Florida mesonet task as the central Florida data deficiency task and proposed the data assimilation model task. The data deficiency task was a scaled-down version of the original mesonet task focusing on the identification of all weather data sources in central Florida that could be used to support operations at the Kennedy Space Center (KSC) and the Eastern Range at Cape Canaveral Air Station (CCAS). The data deficiency and data assimilation model tasks were combined and approved by consensus at the 1997 meeting.

The combined task was originally titled Data Assimilation Model/Central Florida Data Deficiency. In July 1998, the first part of the title was changed from Data Assimilation Model to Local Data Integration System (LDIS). The title change makes it clear that the new AMU task entitled Extend Local Data Integration System is a follow-up effort to the LDIS/Central Florida Data Deficiency task.

There are three primary objectives for the LDIS/Central Florida Data Deficiency task:

- Identify all existing meteorological data sources that lie within 250 km of KSC/CCAS.
- Identify an appropriate data assimilation model that incorporates and analyzes all existing central Florida meteorological data sources.
- Implement a working prototype of the data assimilation model with an appropriate analysis domain and perform a proof of concept test through a post-analysis of selected warm and cool season weather events.

The ultimate goal for running LDIS is to generate products that may enhance weather nowcasts and short-range (< 6 h) forecasts issued in support of the 45th Weather Squadron (45 WS), SMG, and the Melbourne National Weather Service (NWS MLB) operational requirements. The LDIS has the potential to provide added value for nowcasts and short term forecasts for two reasons. First, it incorporates all data operationally available in east central Florida. Second, it is run at finer spatial and temporal resolutions than current national-scale operational models such as the Rapid Update Cycle (RUC; Benjamin et al. 1998) and Eta models. The LDIS combines all available data to produce grid analyses of primary variables (wind, temperature, etc.) at specified temporal and spatial resolutions. These analyses of primary variables can be used to compute diagnostic quantities such as vorticity and divergence. In combination with a suitable visualization tool, LDIS may provide users with a more complete and comprehensive understanding of evolving mesoscale weather than could be developed by individually examining the disparate data sets over the same area and time.

1.2 Report Objectives and Organization

The objectives of this report are to:

- Describe the data availability in central Florida, choice and configuration of the LDIS, and issues associated with prototype installation.
- Present results from post-analyses of two selected cases and the impact of data non-incorporation on the analyses.
- Discuss lessons learned about LDIS added value and identify issues related to running and/or using an operational version of LDIS.

The report is organized as follows. The central Florida data deficiency problem is addressed in Section 2. The choice of an assimilation model and implementation of a working prototype is discussed in Section 3. The fidelity of analyses from the case studies is examined in Section 4 while the utility of these analyses is described in Section 5. In Section 6, results from the data non-incorporation experiments are summarized to document the impact that specific data sources have on the analyses. Finally, the report concludes with a summary of results including lessons learned about the added value of LDIS and issues for future work with LDIS.

2.0 Central Florida Data Deficiency

This section focuses on the identification of all weather data sources in central Florida that could be used to support operations at KSC/CCAS. In fact, the utility of LDIS depends to a large extent on the reliability and availability of both in-situ and remotely-sensed observational data. Therefore, it is important to document all existing meteorological data sources around central Florida that can be incorporated by LDIS. Based on SMG's interest in a Florida mesonet, the discussion also highlights recent efforts by several state and federal agencies to collect and transfer various surface meteorological and hydrological data within Florida in order to produce a state-wide mesonet.

2.1 Data Coverage and Resolution

Data density and coverage in east central Florida varies considerably depending on the level in the atmosphere and distance from KSC/CCAS. All observational data within 250 km of KSC/CCAS that can be incorporated by LDIS are shown in Table 2.1. This table also includes an estimate of the horizontal resolution, vertical extent, frequency of observation, and variables that are measured for each data source. The horizontal resolution of the various data types is estimated from the observations collected for the two case studies discussed in Sections 4 and 5. The horizontal distribution of fixed data locations is shown in Figure 2.1. Fixed data types include all sensors whose geographical locations do not change with time such as the Melbourne (MLB) Weather Surveillance Radar-1988 Doppler (WSR-88D), KSC/CCAS towers and profilers, rawinsonde, buoy, and aviation routine weather report (METAR) stations. The density and coverage of the remaining data types vary considerably as a function of time, weather, etc. and are therefore not shown in Figure 2.1.

Table 2.1. Data availability within 250 km of KSC/CCAS including data type, horizontal resolution, vertical extent, variable(s) observed, and frequency.

Data Type	Horizontal resolution	Vertical Extent	Variables	Frequency (min)
GOES-8 VIS imagery	1 km	---	brightness T	15
GOES-8 IR imagery	4 km	---	brightness T	15
Cloud/WV drift winds	24 km	Variable	u, v	360
METAR	34 km*	Sfc	u, v, T, T_d, p	60
Buoy/ship	34 km*	Sfc	u, v, T, T_d, p, SST	60
Central Florida mesonet	34 km*	Sfc	u, v, T, T_d, p	60
KSC/CCAS towers	4 km	1.8–150 m	u, v, T, RH	5
Rawinsonde	200 km	Sfc to Stratosphere	u, v, T, RH	720
GOES-8 Soundings	30 km	Sfc to Stratosphere	T, q	60
WSR-88D	0.2–1.0 km	Variable$^+$	radial wind, ref, SW	6
Aircraft/pilot reports	Variable	Variable	u, v, T, ICE, TURB, cloud	Variable
ACARS	25 km	Variable	u, v, T	7.5
915 MHz Profiler	11 km**	0.117–3.1 km	u, v, T_v	15
50 MHz Profiler	11 km**	2.0–18.6 km	u, v	5

*Represents the combined horizontal resolution of METAR, buoy/ship, and the central Florida mesonet.
$^+$Depends on radar echoes.
**The combined horizontal resolution of five 915 MHz profilers and one 50 MHz profiler over KSC/CCAS.
u = west-east wind v = north-south wind
T = temperature T_d = dew point T_v = virtual temperature SST= sea-surface temp.
RH = relative humidity q = specific humidity p = pressure ref = reflectivity
ICE = icing TURB = turbulence WV = water vapor SW = spectral width
VIS = visible IR = infrared GOES = Geostationary Orbiting Environmental Satellite
ACARS = Aeronautical Radio, Inc. (ARINC) Communications, Addressing and Reporting System

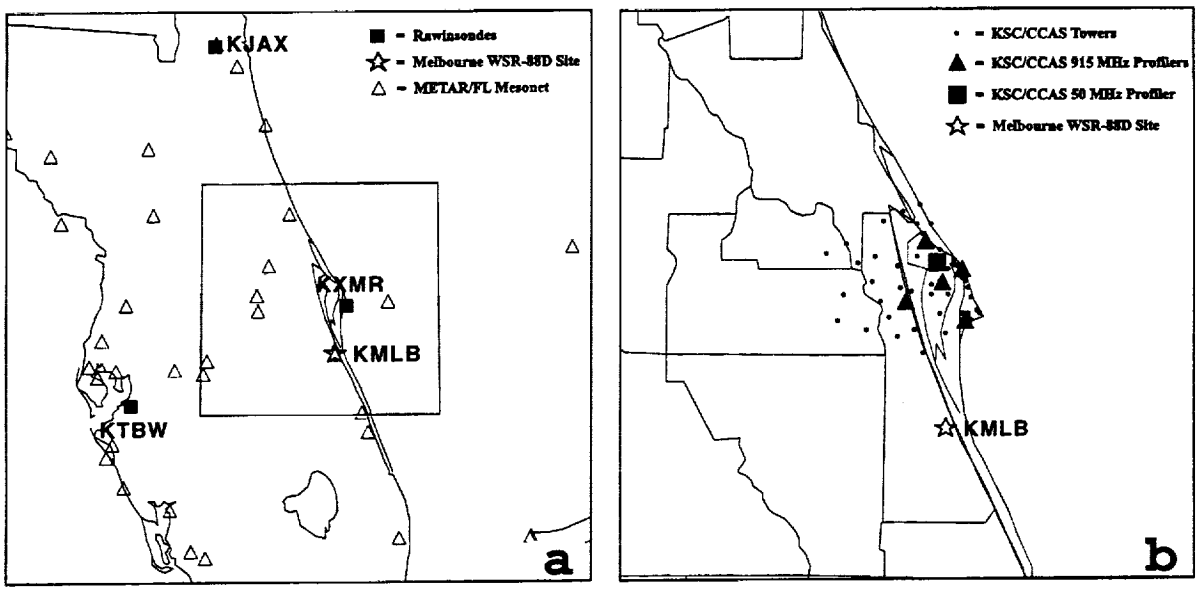

Figure 2.1. Fixed data locations are shown over the Florida peninsula in panel a) for METAR, buoy, and Florida mesonet (open triangles), rawinsondes (solid squares), and the Melbourne WSR-88D (star). Fixed observation sites are given in panel b) for KSC/CCAS towers (dots), 915 MHz profilers (solid triangles), 50 MHz profiler (solid square), and the MLB WSR-88D (star). The inner box in panel a) outlines the extent of the domain shown in panel b).

An examination of Table 2.1 and Figure 2.1 reveals the following:

- The largest variability in horizontal/vertical coverage and density occurs with aircraft data, satellite soundings, and satellite winds.
- The maximum density of near-surface wind and temperature observations occurs within KSC/CCAS.
- WSR-88D, KSC/CCAS towers, and GOES-8 satellite imagery have the smallest horizontal resolution of all data types at < 10 km.
- WSR-88D, KSC/CCAS towers, profilers, ACARS, and GOES-8 satellite imagery provide the greatest frequency of observations at ≤ 15 minutes.
- The three rawinsonde sites at Tampa, Cape Canaveral, and Jacksonville, FL provide the least spatial and temporal resolution of all sensors. However, rawinsondes are the only sensors that provide thermodynamic information from the surface to the lower stratosphere.

The distribution of surface observations from METAR, buoy/ship and Florida mesonet stations shows a concentration over the central portion of the peninsula with almost no surface data available over the western Atlantic (Figs. 2.1a and b). The one 50 MHz and five 915 MHz boundary layer profilers (with Radio Acoustic Sounding Systems) are located around KSC/CCAS and provide high temporal resolution wind and virtual temperature measurements over limited areas (Fig. 2.1b).

Commercial aircraft observations from Pilot Reports (PIREPS) and ACARS data are typically concentrated at flight levels in the upper troposphere and at lower levels during aircraft ascent/descent near airports (Schwartz and Benjamin 1995). The spatial resolution and frequency of aircraft data can vary depending on the time of day, weather conditions, and flight plans. ACARS reports are relayed automatically from the aircraft with a sampling frequency of 7.5 min. The data are available approximately 15 minutes after observation time and

include latitude, longitude, time, temperature, flight level, wind speed, and direction. The precision of temperature and wind speed measurements is estimated to be on the order of 1°C and 0.5 $m\ s^{-1}$, respectively (Schwartz and Benjamin 1995).

Vertical profiles of temperature and moisture are retrieved hourly from GOES-8 sounder data at a horizontal resolution of ~30 km (Gray et al. 1996). However, soundings are available only in cloud-free areas so horizontal coverage can vary depending on the time of day, synoptic conditions, etc. The GOES-8 satellite soundings of temperature and moisture are available in cloud-free areas every hour from the surface to 0.1 mb.

The vertical and horizontal distribution of cloud-drift winds depends primarily on tracking cloud features and diagnosing heights to assign the vertical level for the associated wind (Neiman et al. 1997). The coverage of water vapor (WV) winds also depends on tracer selection and height assignment, although WV wind vector targets are selected in both cloudy and cloud-free regions (Veldon et al. 1997). In contrast to GOES-8 soundings, cloud-drift and WV winds are found where clouds and moisture features can be can be identified by the tracer selection and tracking algorithms (Neiman et al. 1997; Veldon et al. 1997). The cloud drift and WV winds are produced four times per day at 0000, 0600, 1200, and 1800 UTC. Cloud drift winds are assigned heights at high- (100–400 mb), middle- (400–700 mb) and low- (700–950 mb) levels (Nieman et al. 1997) while WV winds are assigned heights at levels between 250–600 mb (Veldon et al. 1997).

The three-dimensional coverage of the MLB WSR-88D depends on the presence of echoes; however, the radar has a maximum horizontal range of several hundred kilometers and a vertical range of 25 km. While the WSR-88D has the best spatial resolution (between 0.2-1.0 km depending on range) and a volume scan frequency of 6 minutes, it provides measurements of only reflectivity, radial velocity, and spectrum width.

Even though several WSR-88D sites could impact LDIS analyses, only MLB WSR-88D level II data were used in this study. In order to include radar observations from other WSR-88D locations, it would be necessary to obtain and process level II data for Jacksonville, Tampa, Miami, Tallahassee, and Key West in addition to MLB WSR-88D. In terms of time and resources, this amount of data processing is beyond the scope of the present study.

Among the measured variables in east central Florida, moisture is the least represented based on the available observations. Table 2.2 summarizes information from the fourth column of Table 2.1 to illustrate the number of data types measuring wind, temperature, and moisture. As shown in Table 2.2, 11 of 13 sensors provide wind data. In contrast, moisture data are available from only 6 of 13 sensors including METAR, buoy/ship, central Florida mesonet, and KSC/CCAS towers that provide moisture measurements in a very shallow layer from the surface to 150 m. However, WSR-88D and GOES-8 satellite imagery can be used in LDIS to enhance the moisture field as discussed in Section 3.3.2.

Table 2.2. Number of data types from Table 2.1 measuring wind, temperature, and moisture variables.

Variable	Number of Data Types
Wind	11
Temperature	9
Moisture	6

2.2 Florida Mesonet Data

In an effort to document all available data in central Florida, the AMU identified two primary sources for surface meteorological and hydrological data within Florida. The first source is the central Florida mesonet listed in Table 2.1 that can be accessed through the web site of the NWS in Tampa (TPA), FL. The data from NWS TPA presently include hourly observations from standard METAR stations, automated surface observing

systems (ASOS), open water and coastal buoys, and other government, agricultural, and utility sites. Real-time data from the NWS TPA web site became available around the beginning of 1997.

The second source consists of two data servers established by the Army Corps of Engineers (ACE) at Jacksonville, FL and the United States Geological Survey (USGS) at Miami, FL. The servers are synchronized in login, password, and directory structure so that they look identical to users. These sites provide a central location for the NWS, USGS, Florida Water Management Districts (FWMD), National Parks Service, and other agencies within Florida to upload and download existing meteorological and hydrological data sets. For example, NWS TPA currently posts their mesonet data to these servers. In addition, the FWMD provide a large number of hourly rainfall and hydrological observations such as river height, discharge rate, etc. Although there are hundreds of FWMD sites, most reports do not include standard meteorological variables such as temperature, wind, pressure, etc. In fact, most of the available data on these servers at the present time include hydrological rather than meteorological information. Real-time data from the ACE and USGS servers became available in March 1998.

Interagency efforts to collect and transfer existing surface meteorological and hydrological data are steps toward establishing a state-wide mesonet. Currently these data can be obtained at no cost through the internet using the information summarized in Table 2.3. Note that details about the sponsor, hostname, data format, etc. listed in Table 2.3 are current as of October 1998. However, access to the data servers and availability of the real-time data files are subject to change at any time. It is important to point out several issues relating to the potential utility of these data for KSC/CCAS operations:

- At present, the majority of data available from NWS TPA are from standard METAR sites. Most of the additional stations comprising the "central Florida mesonet" are concentrated in west central Florida around Tampa (Fig. 2.1a).

- The majority of files currently available on the Miami and Jacksonville servers contain only hydrological observations. Although these data are available at very high spatial resolution, most sites such as those from the FWMD do not provide meteorological observations.

- The meteorological and hydrological data from NWS TPA and the servers are updated hourly which provides the same temporal resolution as standard METAR observations. In addition, these data are available at roughly the same time as standard METAR observations.

- There are relatively few additional meteorological observations within 50 km of KSC/CCAS to supplement the existing METAR and KSC/CCAS tower reports.

Table 2.3. Summary of real-time surface meteorological and hydrological data sources.

	Central Florida Mesonet	**Data Server @ Miami**	**Data Server @ Jacksonville**
Sponsor	NWS Tampa	USGS[1]	Army Corps of Engineers
Point of Contact (POC)	Charlie Paxton	Pat Welsh	Pat Welsh
POC email	Charlie.paxton@noaa.gov	pat.welsh@noaa.gov	pat.welsh@noaa.gov
Access	Web Site	Direct FTP[2]	Direct FTP
Address / Hostname	Http://www.marine.usf.edu	144.42.26.4	155.82.71.71
Username	-----	anonymous	anonymous
Data Format	ASCII	SHEF[3]	SHEF[3]

[1]United States Geological Survey

[2]File Transfer Protocol

[3]Standardized Hydrologic Exchange Format (SHEF; coded ASCII text)

2.3 Availability and Reliability of Real-Time Data

The AMU obtained data needed for this task from various sources as summarized in Table 2.4. It was necessary to use archived rather than real-time data from different sources for the following reasons:

- A number of potential cases were identified in real-time but the actual case selection was performed several weeks later. Since RUC, GOES-8 winds, and GOES-8 sounding data sets were not available in the CCAS Meteorological Interactive Data Display System (MIDDS), these data were obtained from external sources. Although the AMU established real-time access for non-local data sets, the AMU communication bandwidth was not sufficient to download large files in real-time from external sources.

- The real-time AMU archive of local data such as KSC/CCAS towers and METAR observations occasionally failed or was incomplete due to computer and/or communication problems between the MIDDS IBM mainframe and AMU UNIX workstations.

- The AMU did not have access to real-time level II WSR-88D data.

- The real-time AMU access of ACARS data was not available until after the case study dates were chosen. The ACARS data are proprietary and access for this project had to be negotiated and is subject to contractual restrictions.

The AMU acknowledges the points-of-contact listed in Table 2.4 in answering questions and providing data needed for this task. However, an operational version of LDIS will require access to real-time data. As shown in Table 2.5, 8 of the 15 of the data sources are available in real-time from the MIDDS at 45 WS and SMG. Several issues with respect to real-time data for LDIS are discussed below:

- NWS MLB does not currently have access to local data sets such as the KSC/CCAS towers and profilers in their Automated Weather Interactive Processing System (AWIPS). However, these data are available in real-time via modem through the 45 WS MIDDS.

- The RUC grids used as background fields in the analysis (see Section 3) are available on the SMG MIDDS but not on the 45 WS MIDDS. SMG currently receives RUC data on an 80-km grid. When the 45 WS completes the installation of the required hardware and software, RUC data will be available in the 45 WS MIDDS but not at the full 40-km spatial and 1-h temporal resolution. The full resolution RUC grids are available from a NOAA data server at the address listed in Table 2.5.

- The central Florida mesonet data can be obtained from the web site at NWS TPA. However, these data do not currently provide a substantial improvement over the spatial or temporal resolution of existing METAR and KSC/CCAS meteorological observations in east central Florida.

- Access to ACARS data is restricted to authorized users of the NOAA Forecast Systems Laboratory (FSL) web site. However, NWS offices (including SMG) and other government agencies typically have few problems getting permission to access these data.

- The GOES-8 satellite soundings and cloud drift/WV winds are available in real-time from an operational data server at the National Environmental Satellite Data and Information Service (NESDIS). It is possible to ingest raw satellite radiances rather than temperature and moisture retrievals in LDIS using variational objective analysis techniques. However, the LDIS selected for this task does not have that capability so it was not practical to use the raw satellite data (see Section 3).

- The real-time level II WSR-88D data are currently available only at NWS MLB. SMG recently started ingesting real-time level III data into their MIDDS. The level III WSR-88D data are typically obtained from a NEXRAD (NEXt generation RADar) Information Dissemination Service (NIDS) vendor. The advantage of real-time, digital level III data for LDIS is the capability to ingest data from multiple radar sites without the costly requirement for establishing communication pathways to transfer the larger volume of level II data. On the other hand, level III data have less vertical and horizontal resolution than level II data. However, an attempt was not made to simulate the impact of the loss of resolution on the LDIS results.

With the exception of WSR-88D, all other data in Table 2.5 are routinely available in real-time either locally from the 45 WS MIDDS or remotely from external sources. Here the term "routinely" is used to indicate that no potential cases were dropped from consideration due to missing data. In this sense, the real-time data are reliable based on a limited sampling of days. However, no attempt has been made to quantify how often a particular data set is missing from the source location whether on the local MIDDS or the external servers.

The reliability of data can also be judged based on data quality in terms of how often observations are unrepresentative or unrealistic. In general, the archived and real-time data streams described here are not quality controlled (QC'ed) at the source location. For example, KSC/CCAS 915 MHz profiler data are subject to rain contamination as described by Lambert and Taylor (1998). In the presence of rain, lower tropospheric wind profiles from these instruments are erroneous and should be removed from the data set following the procedures discussed by Lambert and Taylor (1998). However, 915 MHz profiler data in MIDDS are not currently QC'ed using this technique, therefore, unrepresentative wind profiles can appear in the real-time data stream. Since there is no guarantee that QC will be performed prior to ingesting data into LDIS, the LDIS should have the capability to handle QC. Specific details regarding QC for archived data used in this task is described in Section 3. In general, the amount of QC and hence reliability of real-time data can vary considerably depending on data type, weather, vertical level of the observation and other factors.

Table 2.4. Summary of archived data sources and points of contact for each data type.

Data Type	Archive Source	Point of Contact
METAR	MESO[1], Inc.	Kenneth Waight
Buoy/ship	NDBC[2] (Buoy only)	Douglas Scally
Central Florida mesonet	NWS TPA	Charlie Paxton
KSC/CCAS Towers	CSR[3]	Susan DeRussy
Rawinsonde	AMU	John Manobianco
ACARS	NOAA FSL[4]	Matt Nitta; William Moninger
PIREPS	NOAA FSL	Matt Nitta; William Moninger
GOES-8 VIS/IR imagery	AMU	Mark Wheeler
GOES-8 soundings	SSEC[5]	Timothy Schmit
GOES-8 cloud drift winds	SSEC	Chris Veldon
GOES-8 water vapor winds	SSEC	Chris Veldon
915 MHz profilers	AMU	Winnie Lambert
50 MHz profiler	CSR	Susan DeRussy
Level II WSR-88D	NWS MLB; NCDC[6]	David Sharp
RUC	ARM[7] Program	Alice Cialella

[1]Mesoscale Environmental Simulations and Operations
[2]National Data Buoy Center
[3]Computer Sciences Raytheon
[4]National Oceanic and Atmospheric Administration Forecast Systems Laboratory
[5]Space Science and Engineering Center
[6]National Climatic Data Center
[7]Atmospheric Radiation Measurement

Table 2.5. Summary of real-time data sources.

Data Type	Real-time Source	Address or Hostname
METAR	MIDDS	-----
Buoy/ship	MIDDS	-----
Central Florida mesonet	NWS TPA	http://www.marine.usf.edu
KSC/CCAS Towers	MIDDS	-----
Rawinsonde	MIDDS	-----
ACARS	NOAA FSL	http://acweb.fsl.noaa.gov
PIREPS	MIDDS	-----
GOES-8 VIS/IR imagery	MIDDS	-----
GOES-8 soundings	NESDIS[1] ORA/FPDT[2]	orbit1a.nesdis.noaa.gov
GOES-8 cloud drift winds	NESDIS ORA/FPDT	orbit1a.nesdis.noaa.gov
GOES-8 water vapor winds	NESDIS ORA/FPDT	orbit1a.nesdis.noaa.gov
915 MHz profilers	MIDDS	-----
50 MHz profiler	MIDDS	-----
Level II WSR-88D	NWS MLB	-----
RUC	MIDDS (SMG only)	140.90.6.103

[1]National Environmental Satellite Data and Information Service
[2]Office of Research Applications/Forecast Products Development Team

3.0 Methodology

This section introduces the warm and cool season cases and provides the reasons for selecting these weather events. Next, the methodology behind choosing an appropriate software package and implementing a prototype LDIS in the KSC/CCAS region is discussed. The prototype data analysis system is described, including the grid configuration, data ingest strategies, and the computational scheme for incorporating observational data. Finally, the available data are presented for the warm and cool season cases.

3.1 Case Study Selection

A case study is selected for both a warm (26-27 July 1997) and a cool season (12 December 1997) event in order to examine the fidelity and utility of wind and cloud parameters in LDIS. Analyses generated from data obtained for each case serve as a basis for the results in this report. The highlights and motivation for selecting each case are given below.

3.1.1 Warm Season Event (26-27 July 1997)

A typical, undisturbed warm season environment characterized the 26-27 July 1997 case. Early in the afternoon, scattered thunderstorms developed across the peninsula and a sea-breeze boundary was evident along the east coast. Later in the afternoon, strong thunderstorms developed southwest of KSC/CCAS and generated an outflow boundary that propagated northeastward. This outflow boundary caused wind gusts greater than 15 m s^{-1} as noted on the KSC/CCAS mesonet towers around 2245 UTC. This case was chosen because the strong winds associated with the outflow boundary forced Atlas launch operation A1393 to be scrubbed for the day.

3.1.2 Cool Season Event (12 December 1997)

The cool season case featured a slow moving cold front accompanied by widespread post-frontal precipitation with embedded thunderstorms. The structure of the wind shift line was detected well by the KSC/CCAS 915 MHz profiler data prior to the onset of precipitation. Northerly winds up to 10 m s^{-1} and widespread low cloud cover followed the frontal passage over KSC/CCAS. The Melbourne WSR-88D indicated a well-defined reflectivity gradient along the leading edge of the front late on 12 December. This case was selected in order to assess the value of LDIS during a weak frontal passage and widespread precipitation event across central Florida.

3.2 LDIS Selection

The two data assimilation systems considered for the LDIS were the Advanced Regional Prediction System (ARPS) Data Analysis System (ADAS; Brewster 1996; Carr et al. 1996) and the Local Analysis and Prediction System (LAPS; McGinley 1995). ARPS/ADAS is available from the Center for Analysis and Prediction of Storms (CAPS) in Norman, OK and LAPS is available from FSL in Boulder, CO. Both LAPS and ADAS can be configured to run at user-defined horizontal/vertical resolutions over any geographical domain. Each system has been used to generate meso-beta scale analyses (~10–30 km) by assimilating a multitude of data that includes aircraft, radar, profiler, satellite, surface, and rawinsonde observations (Stamus and McGinley 1997; Droegemeier et al. 1996).

The ADAS rather than LAPS package was chosen for the prototype LDIS for several reasons. First, at the time when ADAS was selected, ADAS documentation was better than LAPS. ADAS also ingested primarily ASCII data whereas LAPS requires data in netcdf format. Furthermore, LAPS uses a successive correction method (SCM; Bergthorsson and Doos 1955) developed by Barnes (1964) to generate three-dimensional analyses. However, the analyses in ADAS are produced following Bratseth (1986) who developed an iterative SCM that converges to statistical or optimum interpolation (OI). In general, OI schemes are superior to SCM methods because they can account for data density, errors in the data, and dynamical relationships between variables such as the wind components and pressure.

3.3 ADAS Attributes

3.3.1 Objective Analysis Procedure

In order to compute gridded fields of temperature, moisture, and other variables, ADAS uses the Bratseth objective analysis procedure that is a specialized version of the SCM. In the SCM, an analysis is created from a background or first-guess grid and a set of observational data. A background grid typically consists of a large-scale model initialization, analysis, or short-term forecast. The variables at specific grid points are modified from the background values according to observational data located within a specified distance from the grid points. An observation is assigned a weight that is inversely proportional to the distance between the grid point and the observational location. The sum of these weighted observations is added to the background field to generate a new analysis value at the grid point. This process is repeated for all grid points in order to generate the new analysis grid.

The procedure described in the preceding paragraph represents one iteration or pass of the SCM. Several passes can be applied to the background grid in order to fit the observational data more closely or to incorporate different data sources for each pass. During each successive pass, the old analysis value at each grid point becomes the new background value as the correction procedure is repeated. More details on the theory behind SCM and the Bratseth objective analysis scheme are presented in Appendix A.

In ADAS, five variables are analyzed on the ARPS vertical coordinate: u- and v-wind components, pressure, potential temperature, and RH*. RH* is a moisture variable analogous to dew-point depression and is defined as:

$$RH^* = \sqrt{1.0 - RH} \tag{3.1}$$

RH* is selected over specific humidity due to the non-linear change in saturation specific humidity with height. The ARPS vertical coordinate is a terrain-following height coordinate analogous to the traditional sigma coordinate.

3.3.2 Complex Cloud Scheme

One of the features available from ADAS is the Complex Cloud Scheme (CCS) which serves as the basis for moisture data assimilation in the ARPS mesoscale model (Zhang et al. 1998). The CCS is based on LAPS but includes a number of improvements and modifications following Zhang et al. (1998). The CCS incorporates a variety of data and empirically derives a number of cloud and moisture products utilizing a Barnes objective analysis procedure. The Barnes rather than Bratseth scheme is used in the CCS because LAPS was originally developed using a Barnes scheme.

The data used by the CCS are METAR cloud observations, satellite infrared and visible imagery, and radar reflectivity. The products derived from these data include three-dimensional (3D) cloud cover, fractional cloud cover, cloud liquid water (q_c) and cloud ice water (q_i) mixing ratios, cloud and precipitate types, in-cloud vertical velocity, icing severity index, rain/snow/hail (q_r, q_s, q_h) mixing ratios, cloud base, cloud top, and cloud ceiling fields. Furthermore, the CCS enhances the specific humidity (q_v) within areas of analyzed clouds.

The analyzed cloud fields are generated by combining available METAR, satellite, and radar data. METAR and satellite data provide information about the bottom and top of the cloud decks, respectively, whereas radar data fill in the gaps to create a vertically continuous cloud field. Cloud mixing ratios (q_c, q_i) and precipitation mixing ratios (q_r, q_s, and q_h) are determined based on fixed reflectivity thresholds. These thresholds also serve as simple quality control criteria for removing ground clutter. WSR-88D data are linearly interpolated between successive radar beams to provide continuity in the derived cloud fields. Albedo data derived from the visible imagery are primarily used for the removal of excess cloud cover in the analysis (Zhang et al. 1998; Albers et al. 1996).

No data source used in the CCS can provide an actual measurement of cloud thickness. Since there is no information about the thickness of the clouds in the METAR reports, an empirically derived thickness of

roughly 1 km is assigned in the CCS for each cloud layer reported (Albers et al. 1996). The advantage of using METAR observations is that they provide surface-based cloud observations. Therefore, cloud decks can be analyzed by the CCS when they cannot be observed by radar or satellite. For example, high clouds may obscure satellite observations of low clouds or low clouds may form below the lowest elevation angle of the radar beam. One current problem is that standard METAR observations are available only once per hour. Since ADAS is run every 15 minutes as discussed in Section 3.4.1, a discontinuity can occur in the cloud analysis due to the lack of METAR observations at off-hour times.

3.3.3 Automated Data Quality Control in ADAS

An important issue for LDIS involves the quality of data entering into the analysis. Much of the observational data used in ADAS are not quality controlled (QC'ed) at the source location. For this reason, it is important that LDIS performs QC to prevent erroneous data from being used in the analysis.

ADAS contains two algorithms to handle the QC of data incorporated by the analysis scheme. One QC method involves a two-step procedure to check surface observations. First, a time-continuity test is applied to a single surface observation to ensure that it is not drastically different from the previous hourly value. The hourly differences are computed for all stations and for all variables. If any data value lies outside of four standard deviations from the mean of the average hourly differences, then the observation is rejected. Second, the surface data undergo a spatial continuity check. A Barnes objective analysis is performed at the station location using surrounding surface observations. A weighted mean and standard deviation are computed based on these surrounding observations. If the data value in question lies outside of three standard deviations from the mean, then the observation is rejected.

The second method for QC in ADAS compares all observations above the surface to the background grid values interpolated to the observational location. A difference is computed between the observation and the interpolated background value and this difference is compared to pre-determined thresholds for each data source except for surface data. Data that result in differences outside of these threshold bounds are rejected prior to the analysis computation.

The pre-determined thresholds account for instrument errors and the differences in scales of motion resolved by the background field versus the observations. Instrument errors refer to the degree of accuracy in measuring wind, temperature, moisture, etc. associated with a specific type of sensor. Resolution differences are illustrated by considering WSR-88D data versus the RUC analyses. The RUC grid can resolve wind features based on a grid spacing of 40 km. In contrast, the WSR-88D can resolve much finer-scale wind features with its data resolution between 0.2–1.0 km. Therefore, WSR-88D wind observations can be very different from the RUC background values and the QC thresholds are set high to preserve the fine-scale structure of the WSR-88D observations.

A special case of QC was considered for KSC/CCAS wind profiler data. A reduction in the QC thresholds for profiler data was required in the ADAS configuration because the KSC/CCAS 50 MHz data were not QC'ed in the summer case and resulted in erroneous data being incorporated into ADAS. These erroneous 50 MHz profiler winds occurred due to the proximity of heavy precipitation and strong vertical motion associated with vigorous convection which contaminated the retrieval of horizontal winds from this instrument (Schumann et al. 1999). The configuration of ADAS used for the case studies does not distinguish between the 915 and 50 MHz profiler data; therefore, the same threshold was applied to both 915 and 50 MHz KSC/CCAS profiler data. Consequently, some good 915 MHz profiler data in the winter case were rejected by applying more stringent QC for the 50 MHz data.

3.4 ADAS Configuration

3.4.1 Nested Grid Configuration

The configuration of ADAS follows the layout used for the terminal wind analysis in the Integrated Terminal Weather System (ITWS; Cole and Wilson 1995). ADAS is run every 15 minutes at 0, 15, 30, and 45 minutes past the hour, over outer and inner grids with horizontal resolutions of 10 km and 2 km, respectively. The 10-km (2-km) analysis domain covers an area of 500 × 500 km (200 × 200 km) and consists of 30 vertical levels that extend from the surface to about 16.5 km above ground level. The vertical levels are stretched, with the finest resolution near the surface (20 m spacing) and the coarsest resolution at upper levels (~1.8 km spacing). The horizontal coverage and distribution of grid points for both domains are shown in Figure 3.1. Counties are also labeled in Figure 3.1b as a reference for discussions in Sections 4 and 5.

The background fields used on the 10-km analysis domain are the Rapid Update Cycle (RUC) grids of temperature, wind, relative humidity, and geopotential height at 25-mb intervals from 1000 to 100 mb. The RUC analyses are available at a horizontal resolution of 60-km (40-km) every 3-h (1-h) for the warm (cool) season case. The RUC grids are linearly interpolated in time every 15 minutes for each 10-km ADAS cycle. The resulting 10-km analysis grids are then used as background fields for analyses on the 2-km domain. This nested-grid configuration and cascade-of-scales analysis follows that used for terminal winds in ITWS. With such an approach, it is possible to analyze for different temporal and spatial scales of weather phenomena.

The observational data are incorporated into ADAS using multiple passes of the Bratseth scheme to account for the varying spatial resolution of the data sources. Five computational passes are used for the 10-km grid and four passes are utilized on the 2-km grid. Data with similar resolutions are grouped together in the same computational pass such that ADAS incorporates each data source without excessively smoothing the resolvable meteorological features. This methodology ensures that each data source is utilized in ADAS to its maximum potential based on the meteorological features that the data can resolve. The quantitative details regarding the type of data incorporated on each pass are presented in Appendix A.

3.4.2 Data Ingest

The wide variety of observational data used in the LDIS provides measurements at many different times. The version of ADAS used for the LDIS described here is configured to ingest data closest to the analysis time within a 15-minute window (± 7.5 minutes) centered on the analysis time. This data incorporation strategy is designed to simulate one possible operational configuration that would start each cycle after the actual analysis time to allow for the transmission, receipt and processing of real-time data. Alternatively, each cycle could start at the actual analysis time and incorporate all data collected since the previous cycle.

Since the analysis cycle is run every 15 minutes over very fine scales, it is also necessary to ingest some data using non-standard methods. For synoptic-scale analyses, rawinsondes are assumed to provide vertical profiles of moisture, temperature, and winds at a single time and location. However, the balloon can drift a significant distance from the launch site during ascent depending on the speed and direction of the environmental wind. Furthermore, balloons used for upper air measurements ascend at a rate of about 5 m s^{-1} so observations are collected over a period of about one hour. To account for balloon drift, the rawinsonde measurements ingested by ADAS are treated as single-level observations each with an appropriate horizontal and vertical location that is determined using the ascent rate and observed winds. These single-level rawinsonde observations are then grouped into 15-minute bins centered on each analysis time. As a result, only a segment of the rawinsonde profile is used for each analysis cycle.

KSC/CCAS tower data also require a specific strategy to ingest observations into ADAS. Many of the towers provide measurements at multiple levels ranging from 1.8 to 150 m. In order to incorporate tower data in ADAS, multi-level measurements from each tower are treated as soundings. In this way, data from the same tower at multiple levels can be used in the analysis based on fixed observation heights.

Radar observations of reflectivity and radial velocity from the WSR-88D are incorporated into ADAS by averaging all data that fall in each grid volume as described by Brewster (1996) and Albers (1995). Currently, spectrum width data from the WSR-88D are not used by ADAS. Radar observations are rejected if an insufficient percentage of data covers the grid volume or the data have a high variance in the grid volume. Radial winds are unfolded carefully to ensure that the data contributing to the volume average are within the same Nyquist interval. The remapped radial winds are then converted to u- and v-wind component corrections whereas the remapped reflectivity data are converted to moisture variables.

The remapped WSR-88D data are ingested into ADAS based on the time of the volume scan relative to the analysis time. In precipitation mode, the WSR-88D requires approximately 6 minutes to complete a full volume scan. Therefore, each ADAS cycle incorporates the radar scan that begins before the analysis time and overlaps the analysis time.

A similar remapping procedure is applied to GOES-8 visible and infrared satellite data on the 10-km and 2-km grids. The remapped satellite data are used to enhance the analysis of clouds in the CCS as discussed in Section 3.3.2.

3.4.3 Data Availability for Each Case

The data availability for the duration of both case studies is given in Tables 3.1 and 3.2. The warm season case study analyses are generated from 1800 UTC 26 July to 0200 UTC 27 July and the cool season case study analyses are generated from 1300 UTC to 2100 UTC 12 December. The information presented in Tables 3.1 and 3.2 illustrates which data types are used for the analysis cycle at each time. Although GOES-8 visible and infrared images are available in real-time every 15 minutes, the AMU archive is missing some images, especially for the warm season case. With the exception of GOES-8 imagery, the data sets for each case are fairly complete and provide a reasonable representation of data that would be available to run ADAS in real-time. One additional exception is that level II WSR-88D data are currently available in real-time only at NWS MLB (see Section 2.3).

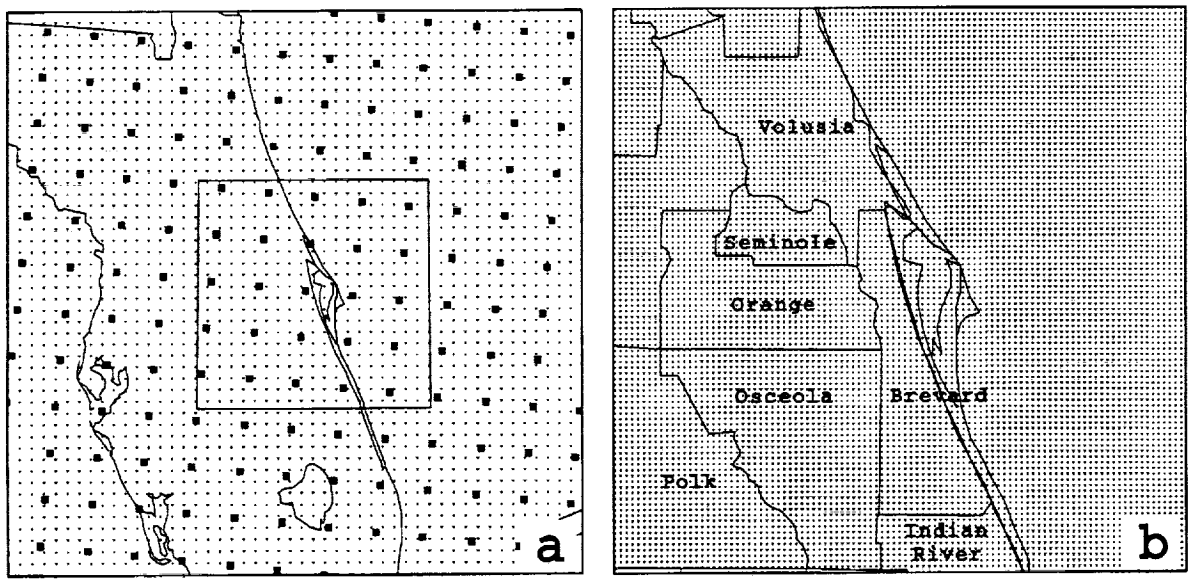

Figure 3.1. The ADAS domains for the 10-km grid and 2-km grid are depicted in panels a) and b), respectively. The 10-km grid point (small dots) and 40-km RUC grid point locations (solid squares) are shown in panel a) while the 2-km grid point locations (small dots) and county labels are shown in panel b). The boxed region in panel a) denotes the 2-km domain.

Table 3.1. Data availability from 1800 UTC 26 July through 0200 UTC 27 July 1997. An 'X' denotes available data whereas a blank entry represents missing data.

Time	ACARS	SATWN	PIREP	Raob	METAR	Tower	SATSN	PROF	IR	VIS	Radar
1800	X	X			X	X	X	X			X
1815	X					X	X	X	X	X	X
1830	X					X	X	X			X
1845	X					X		X	X	X	X
1900	X			X	X	X	X	X		X	X
1915	X			X		X	X	X	X	X	X
1930	X			X		X		X	X	X	X
1945	X			X		X		X			X
2000	X			X	X	X	X	X			X
2015	X					X	X	X			
2030	X					X		X			X
2045	X		X			X		X			X
2100	X		X		X	X	X	X			X
2115	X					X	X	X			X
2130	X					X	X	X			X
2145	X					X		X			X
2200	X				X	X	X	X			X
2215	X					X	X	X	X	X	X
2230	X					X	X	X		X	X
2245	X					X		X	X	X	X
2300	X		X		X	X	X	X		X	X
2315	X					X	X	X	X	X	X
2330	X					X	X	X		X	X
2345	X					X		X	X		
0000	X	X		X	X	X	X	X			X
0015	X			X		X	X	X	X		X
0030	X			X		X		X			X
0045	X			X		X		X	X		X
0100	X			X	X	X	X	X			X
0115	X			X		X	X	X	X		X
0130	X			X		X		X			X
0145	X			X		X		X	X		X
0200	X				X	X	X	X			X

SATWN= GOES-8 cloud/water vapor drift wind
Raob = Rawinsonde
Tower = KSC/CCAS tower
SATSN = GOES-8 satellite sounding
PROF = 915 and 50 MHz profiler
IR = GOES-8 infrared satellite
VIS = GOES-8 visible satellite
Radar = WSR-88D Melbourne

Table 3.2. Data availability from 1300 UTC through 2100 UTC 12 December 1997. An 'X' denotes available data whereas a blank entry represents missing data.

Time	ACARS	SATWN	PIREP	Raob	METAR	Tower	SATSN	PROF	IR	VIS	Radar
1300	X			X	X	X		X			X
1315	X			X		X		X			X
1330	X			X		X		X		X	X
1345	X	X	X	X		X		X		X	X
1400	X				X	X		X	X	X	X
1415	X					X		X		X	X
1430	X		X			X		X		X	X
1445	X					X		X		X	X
1500	X				X	X		X			X
1515	X					X	X	X		X	X
1530	X					X		X		X	X
1545	X					X		X		X	X
1600	X				X	X		X	X	X	X
1615	X					X		X		X	X
1630	X					X		X		X	X
1645	X	X				X		X		X	X
1700	X				X	X		X	X	X	X
1715	X					X		X		X	X
1730	X					X		X		X	X
1745	X					X		X	X	X	X
1800	X		X		X	X		X			X
1815	X		X			X	X	X		X	X
1830	X					X		X			X
1845	X					X		X		X	X
1900	X				X	X		X	X	X	X
1915	X					X		X		X	X
1930	X					X		X		X	X
1945	X	X				X		X		X	X
2000	X				X	X		X	X	X	X
2015	X					X		X		X	X
2030	X					X		X		X	X
2045	X					X		X	X	X	X
2100			X		X	X		X			X

SATWN= GOES-8 cloud / water vapor drift wind
Tower = KSC/CCAS tower
PROF = 915 and 50 MHz profiler
VIS = GOES-8 visible satellite
Raob = Rawinsonde
SATSN = GOES-8 satellite sounding
IR = GOES-8 infrared satellite
Radar = WSR-88D Melbourne

4.0 Fidelity of the LDIS

Because several sources of data are integrated at each analysis time, the fidelity or accuracy of the LDIS needs to be assessed in order to determine if ADAS can depict the same features that are observed from the individual data sets. The goal is to illustrate the accuracy and reliability of the 15-minute analyses and to show that ADAS faithfully represents the observed phenomena. The fidelity is demonstrated through comparisons between the ADAS analyses and actual observations. Wind and cloud features are the focus of this section because these variables are important for operational concerns in east central Florida.

4.1 Wind Fidelity

The outflow boundary in the 26-27 July 1997 case provides a good test to evaluate the accuracy of the ADAS wind analyses. The KSC/CCAS towers capture the evolution and intensity of the outflow boundary as it overspreads KSC/CCAS. At 2300 UTC 26 July, a maximum sustained wind speed of 11 m s^{-1} with gusts of 16 m s^{-1} occurs at KSC/CCAS tower #36 at 27 m (or 90 ft, Fig. 4.1). A steady increase in wind speed precedes this maximum and a gradual decrease occurs after 2300 UTC. The 2-km ADAS wind speeds at 40 m depict the same trend as observed but ADAS shows a maximum of 8.5 m s^{-1} at 2300 UTC which is 2.5 m s^{-1} less than the observed wind at tower #36 (Fig. 4.1).

The ADAS wind speed at 2300 UTC is much greater than the RUC background value of 2.3 m s^{-1} (not shown) due to the incorporation of surrounding observations. It should be noted that this analysis value is not expected to match perfectly the observation at tower #36 due to the influence of several surrounding observations and the fact that ADAS analysis levels do not coincide with the vertical levels of KSC/CCAS towers. With the exception of 2200 UTC and 2300 UTC, the differences between ADAS and tower #36 sustained winds are ~ 1 m s^{-1} or less. Therefore, the ADAS analyzed winds are quite representative of the observations at this specific location.

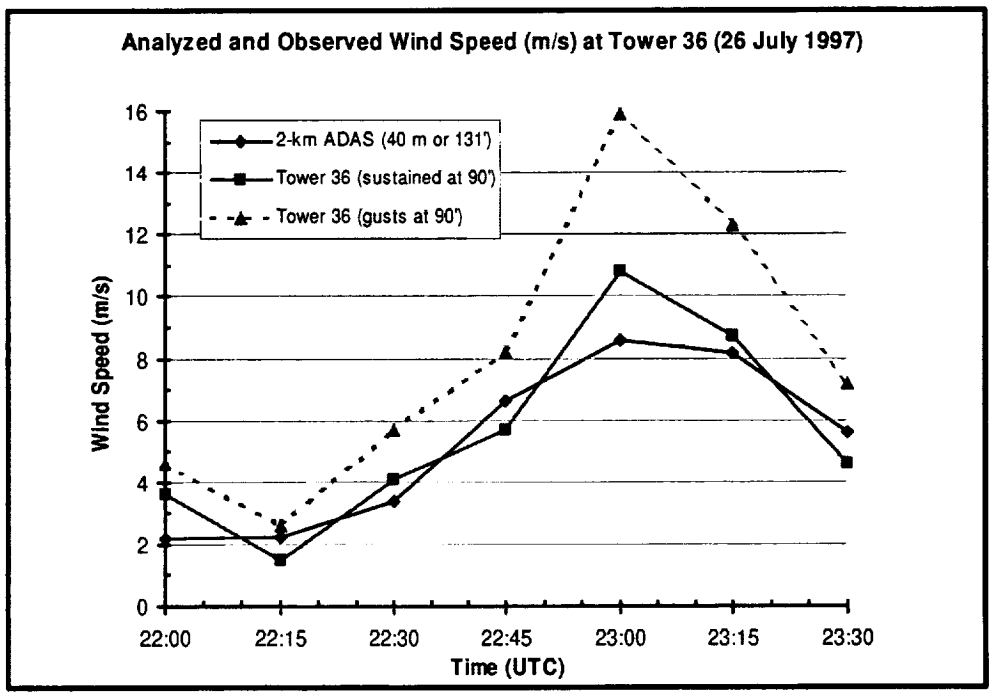

Figure 4.1. A time series of wind speeds (solid line with square labels) and gusts (dashed line) at KSC/CCAS tower #36, and 2-km ADAS winds (solid line with diamond labels) valid from 2200 UTC to 2330 UTC 26 July.

This page intentionally left blank.

In order to assess the fidelity of ADAS analyses incorporating WSR-88D data, the base radial velocities are plotted along with the 2-km ADAS winds at 480 m in Figure 4.2. [The analysis is shown at 480 m because it is the lowest analysis level that experiences a significant influence from WSR-88D data.] These two fields should not be expected to match exactly for two reasons. First, the 2-km ADAS analysis displays winds at a constant height, whereas the WSR-88D image depicts winds on a sloping radar beam. Second, the ADAS total wind speeds are compared to the radial component of the winds in the radar image. Despite these discrepancies, the patterns of maximum winds are consistent with each other in Figure 4.2. Both the ADAS winds (Fig. 4.2a) and radial winds (Fig. 4.2b) depict a maximum in southwesterly winds to the east and southeast of KSC/CCAS.

Another qualitative comparison demonstrates the similarities and differences between 2-km ADAS wind analyses and profiler observations of a cold front passage in the cool season case. Again, an exact quantitative fit to the observations is not expected since the ADAS configuration is not designed to fit the observations perfectly. The winds at KSC/CCAS 915 MHz profiler #4 (Fig. 4.3a) are compared to the 2-km ADAS-analyzed winds interpolated to the profiler site (Fig. 4.3b).

A wind shift from southwesterly to northwesterly characterizes the cold front at KSC/CCAS profiler #4 (Fig. 4.3a). Southwesterly winds extend from the lowest measured level (~117 m) to 1000 m between 1330 UTC and 1530 UTC. A wind shift to northwest occurs thereafter and deepens to the 500-m level shortly after 1700 UTC. Northwesterly winds increase up to 10 m s^{-1} in the 200–500 m layer after the wind shift deepens between 1700–1800 UTC (Fig. 4.3a).

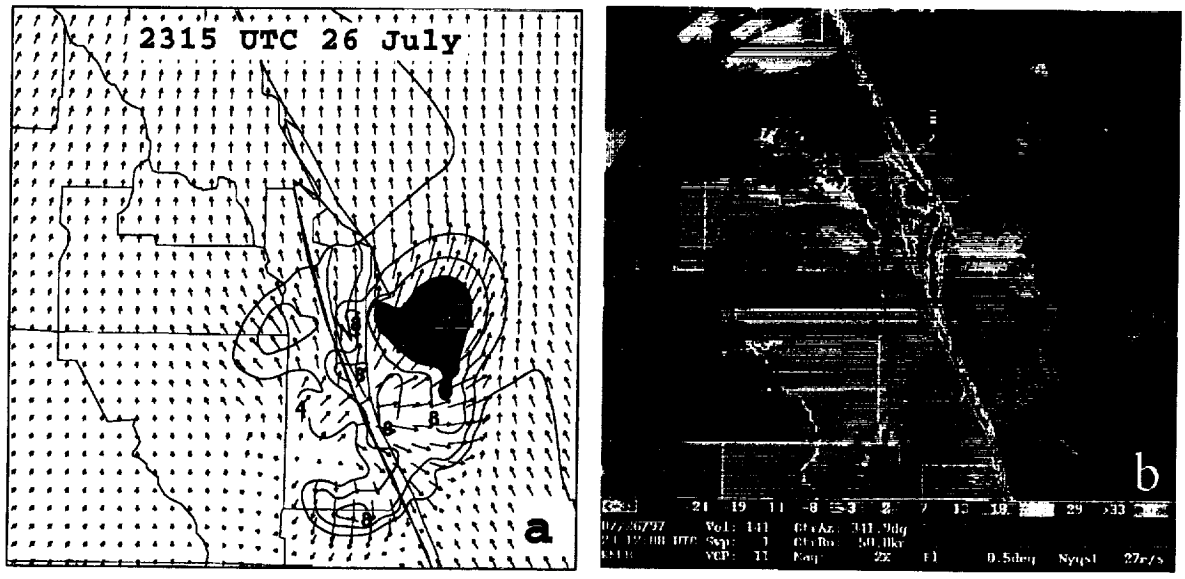

Figure 4.2. The 2-km ADAS 480-m wind analysis at 2315 UTC 26 July and the corresponding Melbourne WSR-88D base velocity at 2312 UTC are shown in panel a) and b), respectively. ADAS wind speeds are contoured every 2 m s^{-1} and shaded above 10 m s^{-1} in a). The bright red shades southeast of KSC/CCAS represent radial velocity greater than 13 m s^{-1} in b).

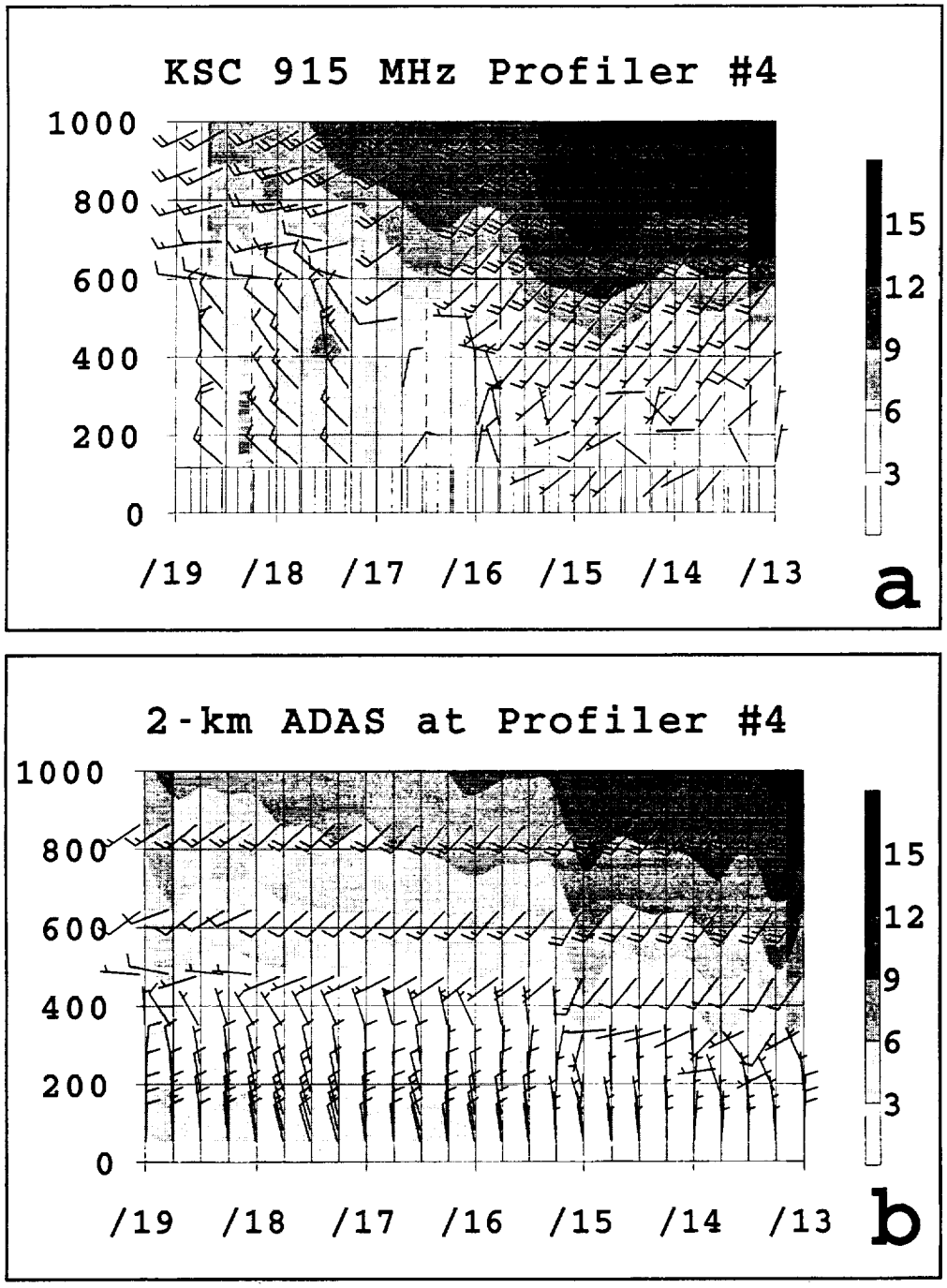

Figure 4.3. A time-height cross section of wind speeds and wind barbs for a) KSC 915 MHz profiler #4 and b) 2-km ADAS analyses interpolated to the location of profiler #4. Wind profiles are plotted every 15 minutes from 1300 UTC to 1900 UTC 12 December with time increasing from right to left. Wind speed is shown in m s^{-1} according to the shading scheme while wind barbs are plotted in m s^{-1} (half barb=2.5 m s^{-1}, full barb=5 m s^{-1}).

A similarity between the profiler data and the ADAS analyses is the maximum wind speeds from 1300–1500 UTC in the layer between 600–1000 m (Fig. 4.3). Another similarity is the minimum wind speed that accompanies the frontal zone between 1500 UTC and 1700 UTC in the 200–400 m range. However, substantial differences occur between the time-height display of winds from the profiler and ADAS analyses most notably between 200–500 m after 1700 UTC. Some possible causes for these differences include:

- ADAS does not exactly fit point observations due to the influence of surrounding observations and the weighting scheme that accounts for errors in the observations and background fields.

- Observations incorporated into ADAS have an influence on surrounding grid points in three-dimensions based on specified horizontal and vertical influence distances (see Appendix A). In the case of KSC/CCAS profiler data, a small vertical influence range is chosen to prevent the 915 MHz data at lowest levels from affecting the surface analysis in ADAS. Therefore, a small vertical influence range in regions of mismatched vertical levels can cause profiler data to have a limited influence on the ADAS analysis.

A mismatch between the vertical distribution of the analysis levels and observation levels occurs because ADAS uses a stretched vertical coordinate, whereas data from the KSC/CCAS 915 MHz profilers are at fixed intervals (~100 m). An example of such a mismatch occurs between 200–500 m in the region characterized by substantial differences between the analyzed and observed wind profiles (Fig. 4.3). Further experimentation is necessary to determine whether a different configuration of ADAS can resolve the problems of mismatched vertical levels in a variety of weather situations.

The shallow nature of the wind shift line is an important aspect of the 12 December cold front. The surface frontal passage occurs before 1300 UTC at KSC/CCAS based on METAR and tower observations (not shown). However, the frontal wind shift is generally ≤ 200 m deep from 1300–1530 UTC according to the profiler data (Fig. 4.3a). Southwesterly winds are measured above 117 m between 1400–1500 UTC despite northerly winds indicated by surface observations (not shown).

A benefit of ADAS in this scenario is that the lowest analysis level (10 m) is closer to the ground than the lowest profiler level (~ 117 m). In addition, ADAS integrates surface and low-level data in the form of METAR and KSC/CCAS tower observations, respectively. Therefore, ADAS can analyze the shallow wind shift below 200 m between 1300 UTC and 1500 UTC that can not be observed by the 915 MHz profilers.

4.2 Cloud Fidelity

This section provides a qualitative verification of the derived fractional cloud cover and cloud top heights of the 10-km analyses for the warm and cool season cases and the 2-km analyses for the warm season case. The 1-km GOES-8 visible imagery is used for comparison with the fractional cloud cover while 4-km GOES-8 infrared (IR) imagery is used for comparison with the cloud top heights. The CCS products should not be expected to match the GOES-8 patterns exactly because the CCS products represent different fields than the GOES-8 brightness temperature images.

For the warm season case, the area of convection southwest of KSC/CCAS is examined at 2215 UTC near the time of its peak intensity. The highest cloud fractions (> 0.8 in Fig. 4.4a) correspond closely with widespread and textured clouds on the visible imagery (Fig. 4.4b) which represent areas of heavy thunderstorms in central Florida. Other features common between Figures 4.4a and b include the cluster of thunderstorms along the Georgia/Florida border, the two isolated cells north of KSC/CCAS along the coast and offshore, and the band of clouds west and southwest of Lake Okeechobee.

The derived cloud top heights compare favorably with the GOES-8 IR imagery. Similar patterns and features are evident in both the image of cloud top heights (Fig. 4.4c) and brightness temperatures (Fig. 4.4d). Cloud tops greater than 14 km occur to the southwest of KSC/CCAS and in extreme northern Florida near the Georgia border. These same areas have the greatest enhancements on the IR display (brightest shades of gray in Fig. 4.4d).

This cloud verification is also presented for the cool season case at 1400 UTC 12 December. Figure 4.5a depicts widespread cloudiness (fractions > 0.9) over much of central and northern Florida. This cloud fraction field agrees qualitatively with the GOES-8 visible imagery (Fig. 4.5b) which indicates extensive cloud cover over most of the Florida peninsula. Gaps in the cloud cover occur over extreme northwestern Florida and north of Lake Okeechobee in both Figures 4.5a and b. Also, smaller cloud fractions occur over southern Florida where visible imagery depicts thinner clouds.

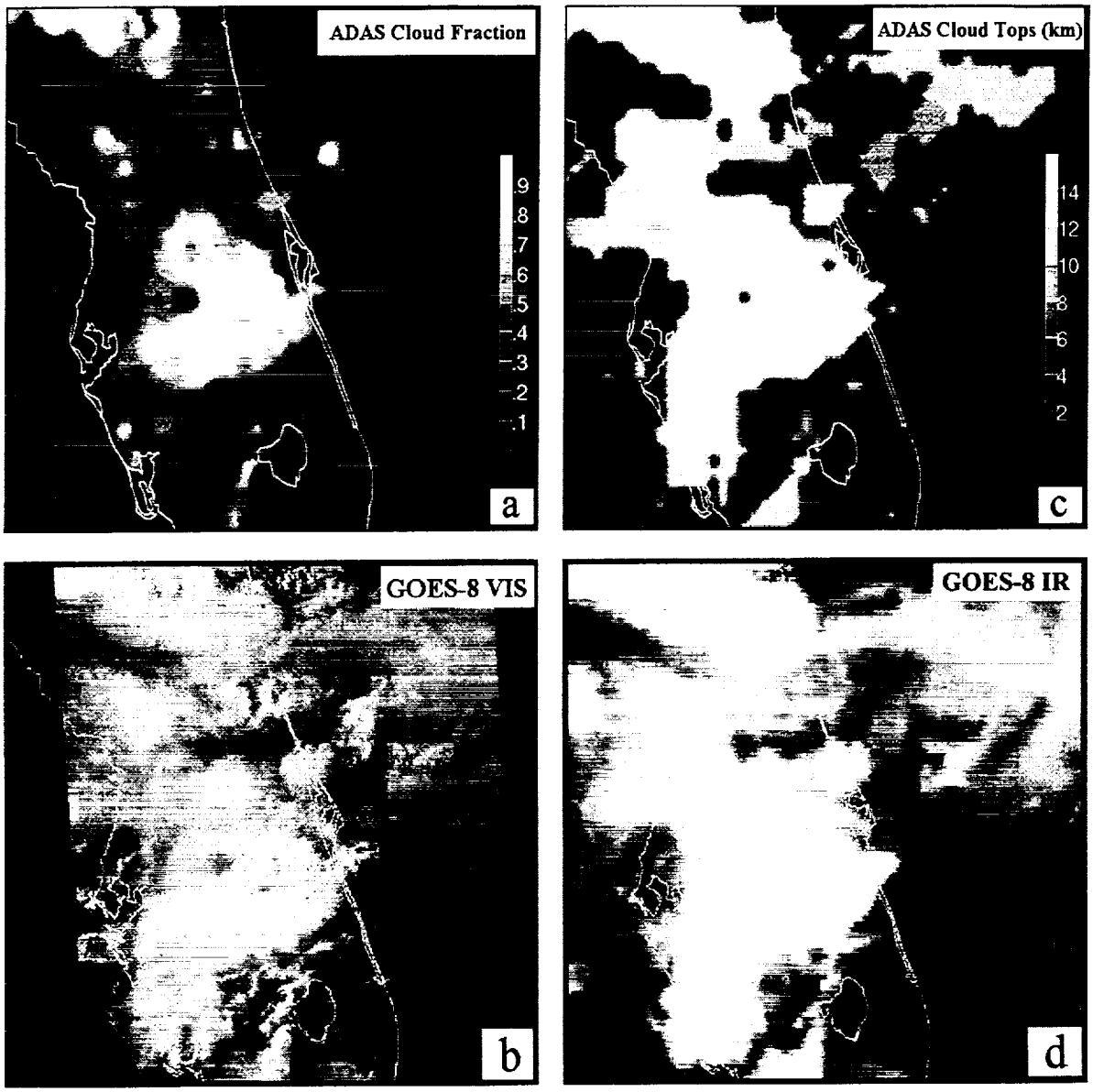

Figure 4.4. The 10-km ADAS cloud fraction, GOES-8 visible, 10-km ADAS cloud top heights, and GOES-8 infrared images are given in panels a), b), c), and d), respectively, valid at 2215 UTC 26 July. Progressively brighter gray shades represent an increase in 10% (0.1) cloud cover in panel a) while progressively brighter gray shades represent an increase in cloud top heights by 2 km (brightest shade > 14 km) in panel c).

This widespread cloudiness results partly from a large cluster of thunderstorms that developed early on 12 December over the eastern Gulf of Mexico. These storms produced a southwest–northeast elongated anvil across much of central and northern Florida by 1400 UTC as evident in Figures 4.5c and 4.5d. The highest derived cloud tops (> 12 km; Fig. 4.5c) and coldest brightness temperatures on the IR image (Fig. 4.5d) occur over much of the central and northern Florida and the eastern Gulf of Mexico. The cloud top height field also captures the small gap in cloud cover north of Lake Okeechobee and the low cloud tops over southeastern Florida (Fig. 4.5c).

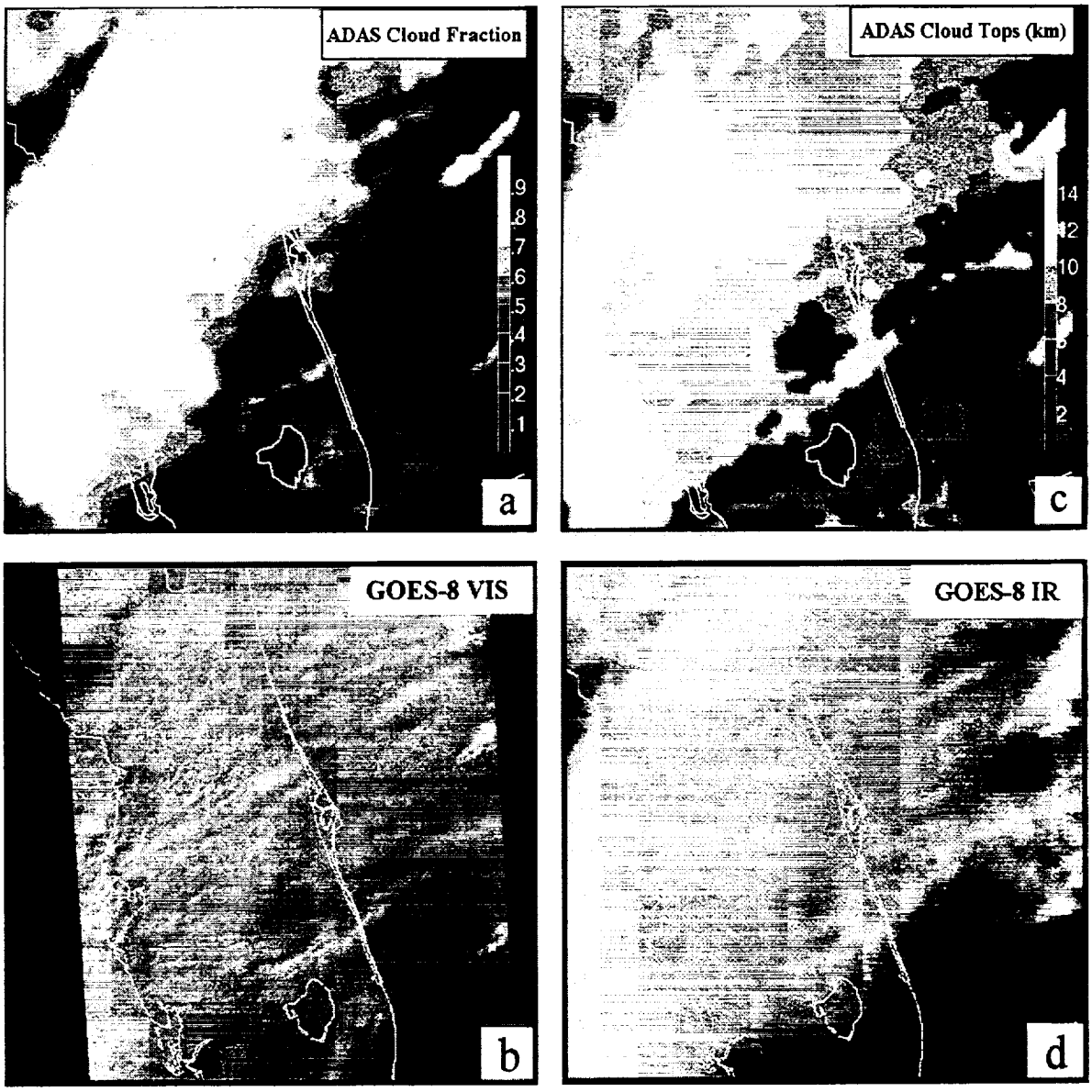

Figure 4.5. The 10-km ADAS cloud fraction, GOES-8 visible, 10-km ADAS cloud top heights, and GOES-8 infrared images are given in panels a), b), c), and d), respectively, valid at 1400 UTC 12 December. Progressively brighter gray shades represent an increase in 10% (0.1) cloud cover in panel a) while progressively brighter gray shades represent an increase in cloud top heights by 2 km (brightest shade > 12 km) in panel c).

The examples from the 10-km ADAS analyses discussed in the previous paragraph demonstrate a reasonable qualitative fit to the GOES-8 imagery; however, the 2-km cloud fields from the warm season case depict more fine-scale details. The ADAS 2-km cloud fractions and cloud top heights are also shown at 2215 UTC 26 July (Fig. 4.6). The increased detail over the 10-km cloud fields is clearly evident. Note the circular convective cell in the 2-km fields north of KSC/CCAS (Fig. 4.6) as compared to the irregular shape of the 10-km fields (Figs. 4.4a and c). This circular feature more closely resembles the visible and IR images in Figures 4.4b and d, respectively. Remapping 1-km GOES-8 visible and 4-km GOES-8 IR data to the coarser 10-km ADAS grid causes the "blockiness" of the cloud fields. This remapping procedure results in a slight loss of resolution on the 10-km grid whereas the 2-km grid can retain more details from the GOES-8 imagery.

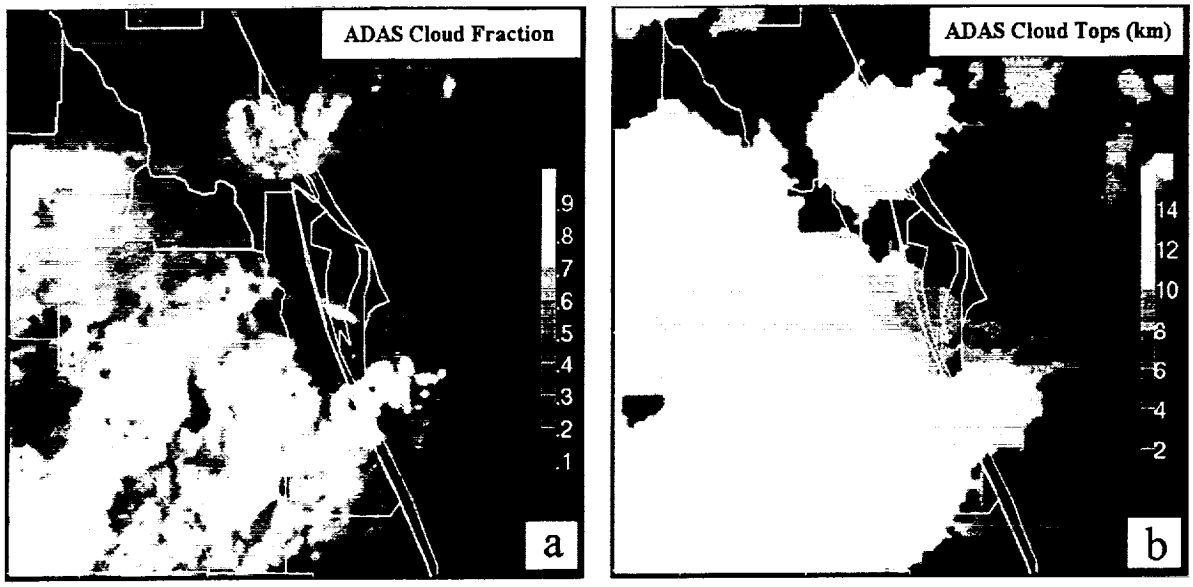

Figure 4.6. The 2-km ADAS cloud fraction and cloud top heights are shown in panels a) and b), respectively. Progressively brighter gray shades represent an increase in 10% (0.1) cloud cover in a) and progressively brighter gray shades represent an increase in cloud top heights by 2 km in b) with the brightest shade > 14 km.

5.0 Utility of the LDIS

The utility of the LDIS is given by the value or usefulness that it can provide through analysis products that are not typically available to weather forecasters. The added value of the LDIS is demonstrated by examining results from both the warm and cool season case studies. The evolution of the 26 July 1997 outflow boundary is presented by utilizing wind and divergence results from the 2-km ADAS. The contributions from individual data sources are illustrated in cross sections of wind speed. In the cool season case, the frontal zone is discussed and the influence of using different background grids is examined. Finally, a variety of derived cloud products illustrate the usefulness of the Complex Cloud Scheme (CCS) of ADAS.

5.1 Diagnosis of an Outflow Boundary

Using the fine-scale results of the 2-km ADAS analyses, the evolution of the wind speeds and wind vectors at 480 m (Figs. 5.1a-d) illustrates the formation and intensification of an outflow boundary during the late afternoon of 26 July. Wind speeds greater than 8 m s^{-1} develop over the Brevard/Osceola county border at 2215 UTC 26 July (Fig. 5.1a) and spread radially over the next 45 minutes. The maximum winds (> 12 m s^{-1}) move northeastward into KSC/CCAS and offshore regions of central Brevard county by 2245 UTC (Fig. 5.1c), the approximate time that the Atlas launch was postponed.

Examination of level II radar reflectivity and radial velocity data (not shown) indicated that features present in the high-resolution wind analyses (Fig. 5.1) are consistent with the scale and motion of patterns associated with the observed thunderstorm. It should be noted that the detailed structure of horizontal winds associated with this boundary would likely be easier to visualize in real-time using ADAS rather than WSR-88D radial velocity displays alone.

Cross sections taken along lines oriented southwest–northeast in Figure 5.1 help to illustrate the vertical structure and evolution of wind speeds analyzed on the 2-km domain. A core of relatively strong winds (8–10 m s^{-1}) associated with the convection to the southwest of KSC/CCAS extends from near the surface to 3000 m at 2215 UTC (Fig. 5.2a). At 2230 UTC, a separate low-level wind maximum with speeds greater than 6 m s^{-1} develops between 200 m and 500 m ahead of this core (Fig. 5.2b). Fifteen minutes later, this low-level wind maximum advances northeastward (left-to-right along the cross section) and increases in intensity to greater than 10 m s^{-1} (Fig. 5.2c). By 2300 UTC, the winds between 1000 m and 3000 m weaken but the low-level wind maximum maintains its intensity. Also at this time, a third wind maximum becomes evident in the 0–200-m layer on the right side of Figure 5.2d.

Above 200 m, surface data do not influence the analyses. Therefore, changes in the horizontal wind field above the surface develop primarily in response to WSR-88D radial velocities in areas where radar reflectivity targets are available. The wind maximum between 200–500 m at 2300 UTC (Fig. 5.2d) shows a gradual upward tilt from southwest to northeast (left to right). This feature results from the incorporation of radar data which slopes upward away from the radar site. Furthermore, note that the winds are less than 6 m s^{-1} between the tilted wind maximum and the wind maximum in the lowest 200 m. These weaker winds are located at levels below the influence of radar data but above the influence of near-surface KSC/CCAS tower data. Therefore, the background winds from the 10-km analysis are retained and the two features are distinct. However, if data were available to fill in this gap, the outflow boundary would likely be analyzed as a single continuous feature from the surface to 1000 m, in advance of the mid-level wind maximum (1000-3000 m) associated with the dissipating thunderstorm.

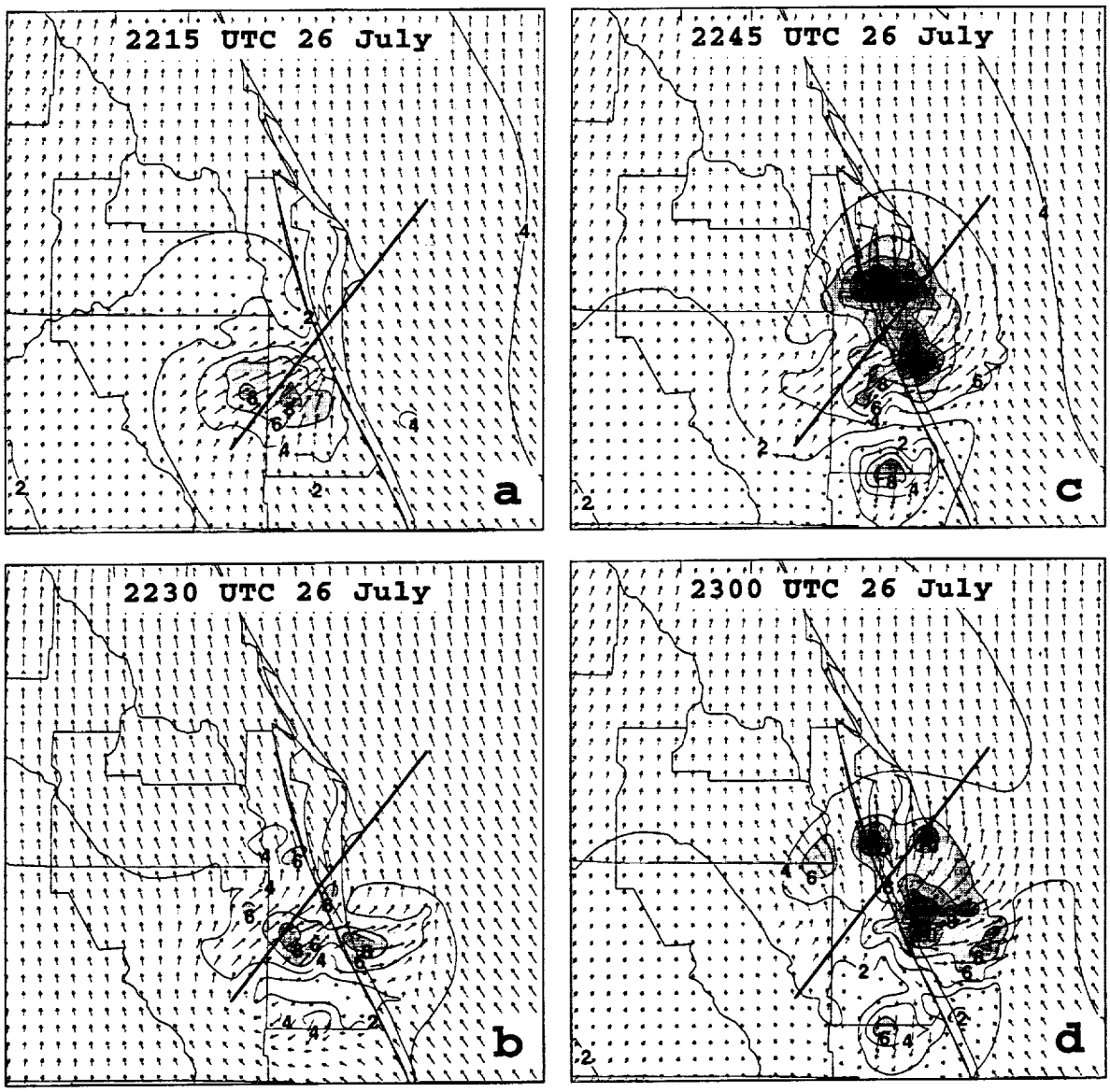

Figure 5.1. A display of the 2-km ADAS wind speed and wind vectors at 480 m. Wind speed is contoured every 2 m s^{-1}, shaded above 6 m s^{-1}, while wind vectors are denoted by arrows. Valid times are a) 2215 UTC, b) 2230 UTC, c) 2245 UTC, and d) 2300 UTC 26 July.

The evolution of the thunderstorm outflow can also be examined through the divergence of the horizontal wind on the 2-km ADAS grid. In Figure 5.3, plots of convergence (shaded), divergence (dashed lines), and horizontal winds are shown at 650 m. At 2215 UTC, an area of convergence is found over much of central Brevard county along the leading edge of the developing outflow boundary (Fig. 5.3a). Weak divergence is also found over northeastern Osceola county at this time. Fifteen minutes later, an extensive area of low-level divergence develops in southern Brevard county, behind the significant outflow boundary (Fig. 5.3b). Convergence along the outflow boundary spreads outward into central Brevard county (just south of KSC/CCAS), offshore of southern Brevard county, and into Indian River county. Divergence continues to intensify across much of interior Brevard county over the next 30 minutes beneath the dissipating thunderstorm (Figs. 5.3c and d), while the band of convergence spreads out radially along the leading edge of the outflow boundary.

By 2300 UTC, a well-defined band of convergence arcs from northern Osceola county, across eastern Orange and northern Brevard county, into the offshore waters of Brevard county, and then back onshore in Indian River county (Fig. 5.3d). Strong divergence exceeding 8×10^{-4} s^{-1} occurs over east-central Brevard county. A cross section through this maximum in low-level divergence at 2300 UTC reveals some interesting structure as shown in Figure 5.4. A large area of strong mid-level convergence is depicted above the low-level divergence maximum in the center of Figure 5.4a. The low-level convergence associated with the outflow boundary is also seen on the far left and far right of Figure 5.4a between the surface and 1000 m. In Figure 5.4b, the vertical velocity field reveals significant sinking motion exceeding -150 cm s^{-1} between 2250 m and 5750 m above the strong low-level divergence depicted in Figure 5.4a. The structure of the circulation closely resembles a downburst scenario, with strong sinking motion above the ground and lateral spreading of the horizontal winds near the surface (Fig. 5.4b).

The ability to analyze convection and its associated outflow in this manner demonstrates the value of LDIS such as ADAS. These detailed products are not possible with the coarser spatial and temporal resolutions of large-scale model analyses such as the RUC or Eta. Furthermore, it is noticeably easier to diagnose and visualize the outflow boundary using ADAS analyses rather than strictly radial velocity data at multiple elevation angles. The combination of 15-minute analyses and the incorporation of data with high spatial and temporal resolution onto a 2-km grid allows for ADAS to capture the fine scale details of an outflow boundary.

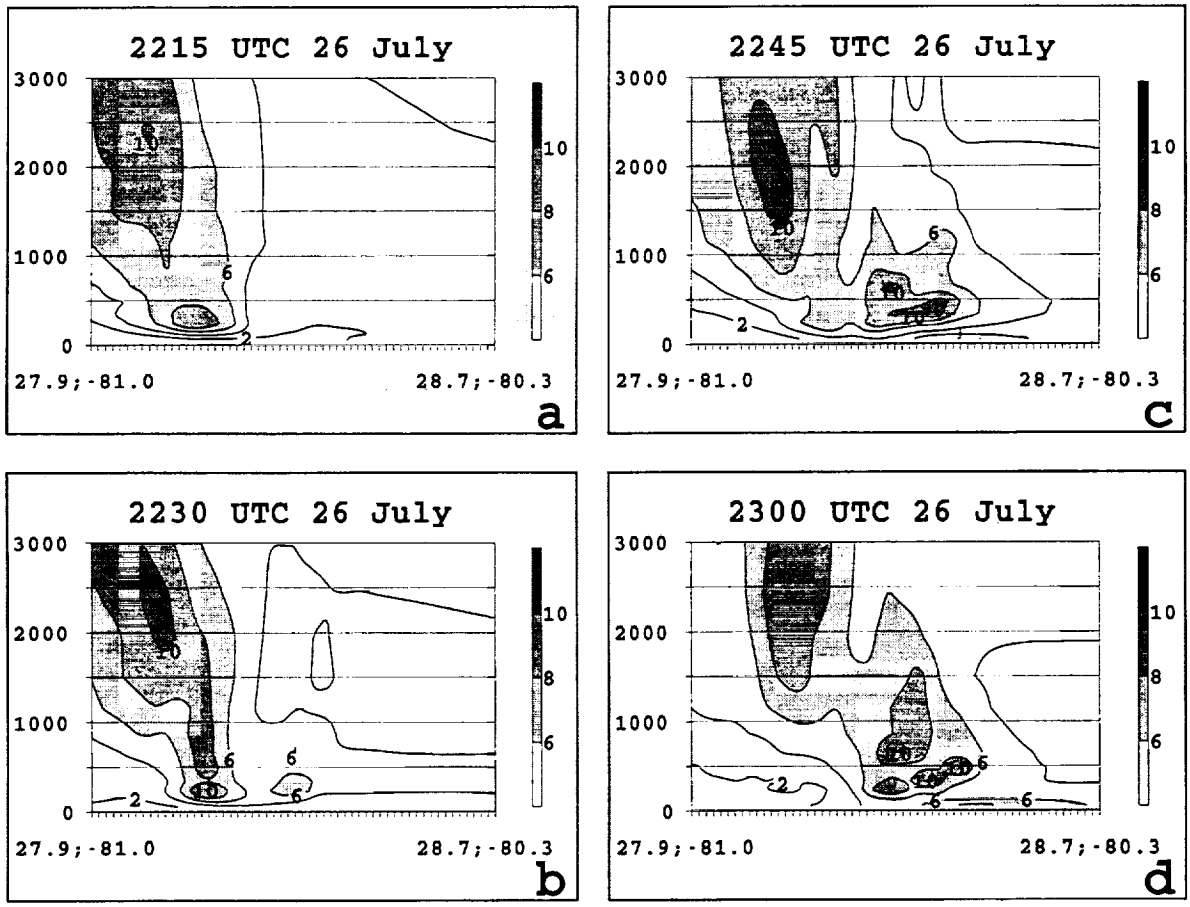

Figure 5.2. A southwest–northeast cross section of wind speeds on the 2-km ADAS grid with winds > 6 m s^{-1} shaded according to the scale provided. The orientation of the cross section is denoted in Figure 5.1. Valid times are a) 2215 UTC, b) 2230 UTC, c) 2245 UTC, and d) 2300 UTC 26 July. The vertical axis extends from the surface to 3000 m.

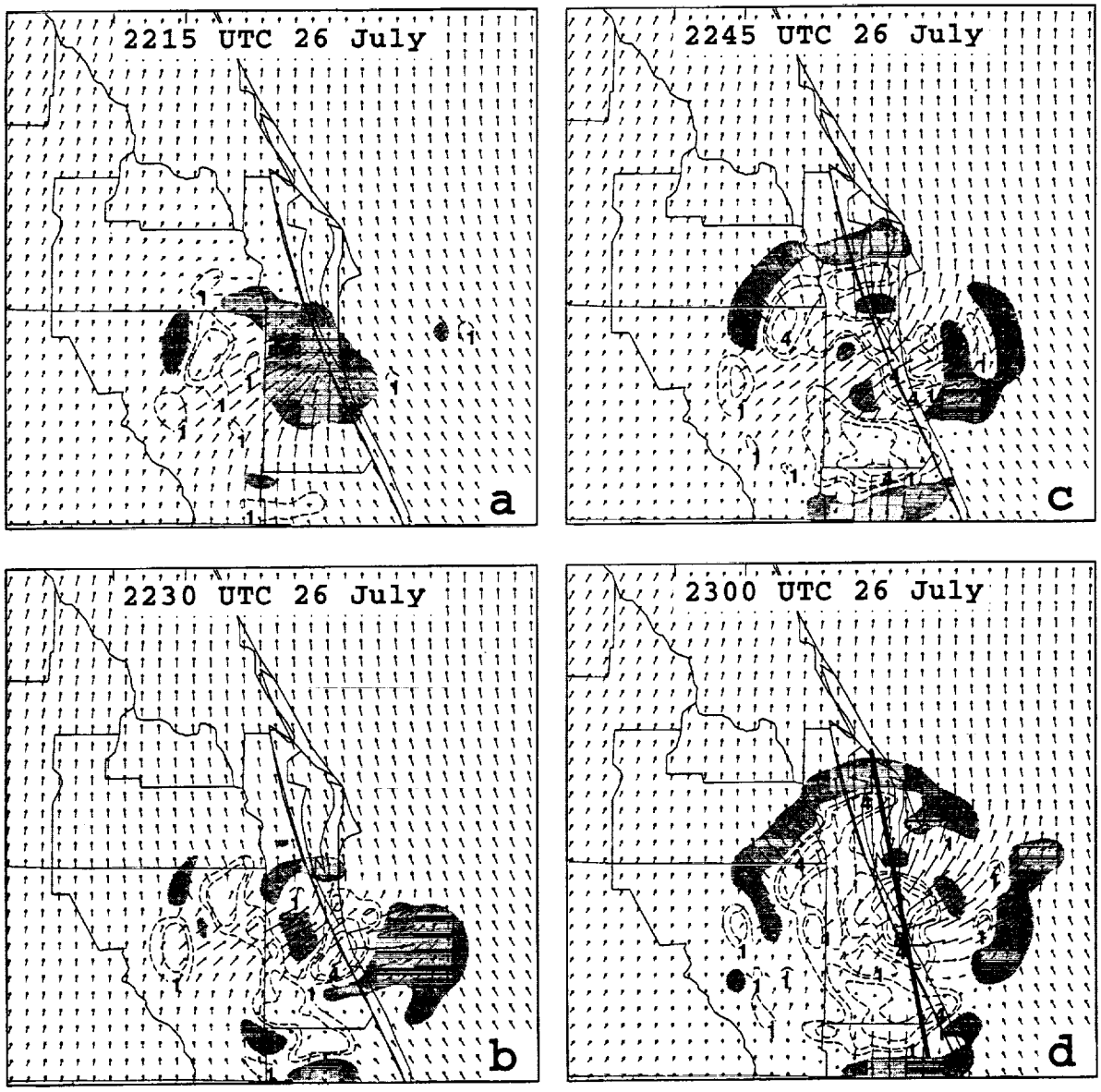

Figure 5.3. Divergence of the horizontal wind ($\times 10^{-4}$ s^{-1}) and wind vectors at 650 m derived from the 2-km ADAS grids. Dashed lines indicate divergence and shading indicates convergence. Valid times are a) 2215 UTC, b) 2230 UTC, c) 2245 UTC, and d) 2300 UTC 26 July.

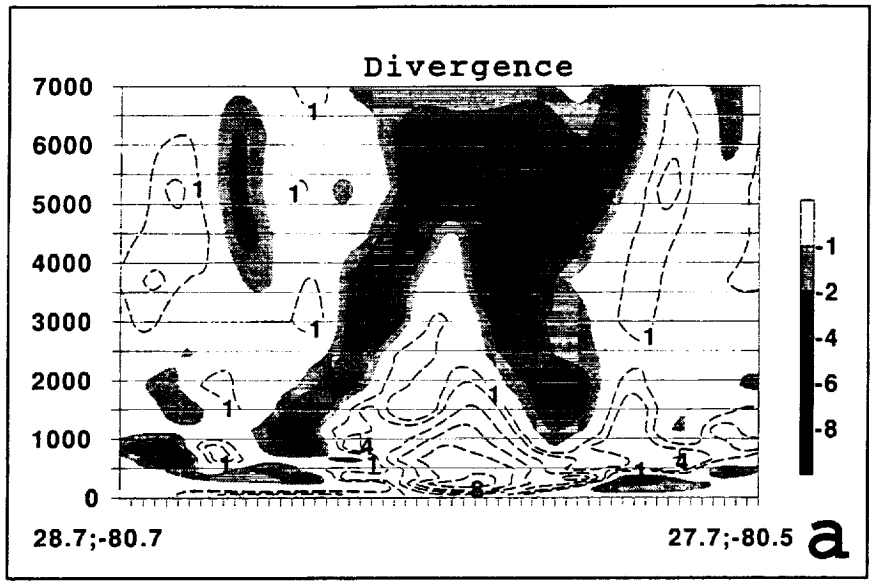

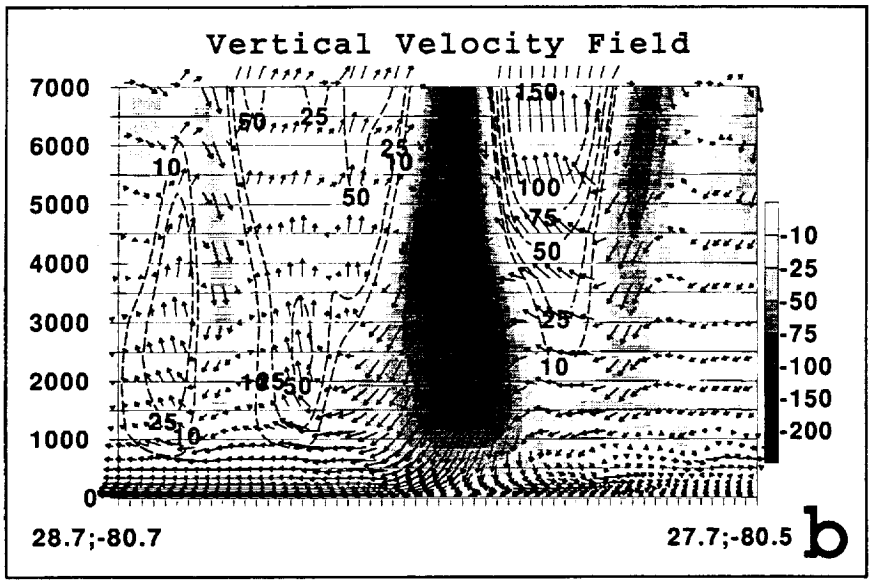

Figure 5.4. Cross section of a) divergence and b) vertical velocity/circulation (derived from the 2-km ADAS grids) at 2300 UTC 26 July 1997 along the line indicated in Figure 5.3d. Dashed lines denote divergence of the horizontal wind field and convergence is shaded according to the scale provided in panel a). Vertical velocity (cm s^{-1}) and the sense of the vertical circulation given by arrows are shown in panel b). The vertical axis ranges from 0 to 7000 m in both panels. Rising motion is indicated by dashed contours while shading represents sinking motion according to the scale provided. Vertical velocities are scaled by a factor of 100 to depict circulation in the plane of the cross section.

5.2 Influence of Different Background Grids

In the cool season case study, the opportunity exists to compare the ADAS analyses using a 40-km versus a 60-km RUC background field. To orient the reader, a plot of the 2-km ADAS streamlines from 40 m at 1400 UTC 12 December is shown in Figure 5.5. A frontal zone lies across central Brevard and northern Osceola counties as indicated by the deformation zone in the wind field. A northerly wind component occurs north of the frontal zone while southwesterlies predominate south of the wind shift. The cold front at 40 m lies south of KSC/CCAS at 1400 UTC (Fig. 5.5). However, southwesterly winds occur just a few hundred meters above the surface as indicated by profiler #4 (Fig. 4.3a) and the other 915 MHz profilers (not shown). The cold front deepens after 1500 UTC across KSC/CCAS but remains less than 600 m deep throughout the entire analysis time window (refer to profiler #4 in Fig. 4.3a). Cold temperature advection is generally weak behind the surface front with the coolest air located over inland areas (not shown).

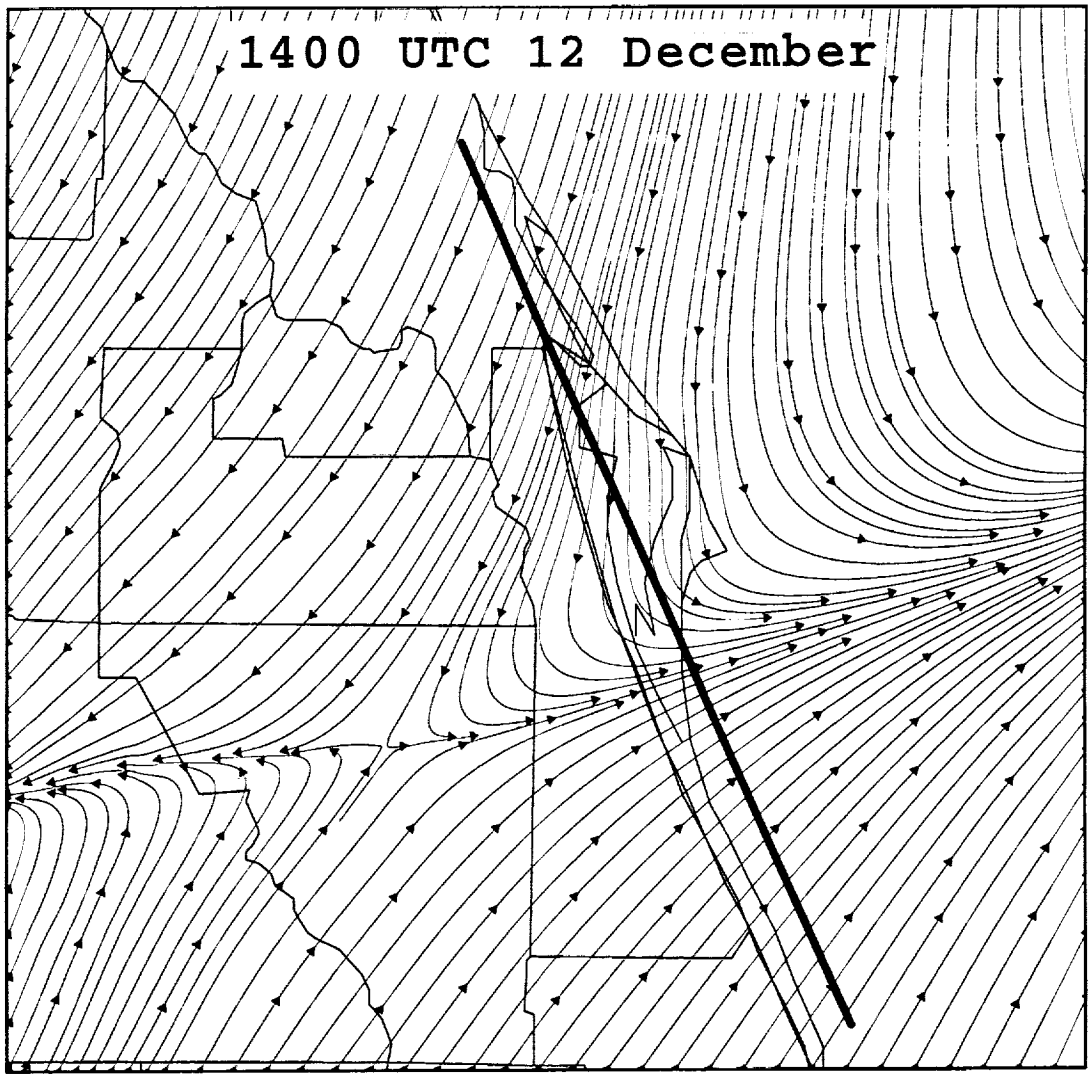

Figure 5.5. Streamlines at 40 m from the 2-km ADAS analysis grid generated by using the 40-km RUC background field valid at 1400 UTC 12 December. The heavy solid line indicates the cross section shown in Figure 5.6.

In order to depict the influence of different background fields, the 10-km ADAS analyses are regenerated using the 60-km instead of the 40-km RUC as a background grid. These new 10-km analyses are then used as background grids for a series of new 2-km ADAS analyses. The new 2-km analyses are compared to the original 2-km analyses to identify the impact of different RUC background fields.

A series of cross sections showing wind speed and tangential wind components are generated for both 2-km analyses and RUC background fields (Fig. 5.6). The location of the frontal zone is near the zero isopleth of tangential winds since this isopleth marks the transition between southerly (negative) and northerly (positive) winds. In Figures 5.6a and b, both the 60-km RUC and the corresponding 2-km ADAS analysis depict tangential wind speeds less than 3 m s^{-1} behind the frontal zone. However, the 40-km RUC and its corresponding 2-km ADAS analysis both show wind speeds of 4–8 m s^{-1} and tangential wind components > 4 m s^{-1} behind the cold front. Due to its finer horizontal and vertical resolution, the 40-km RUC is more capable of resolving the higher wind speeds behind the front as observed at the surface locations behind the cold front (4–5 m s^{-1}, not shown).

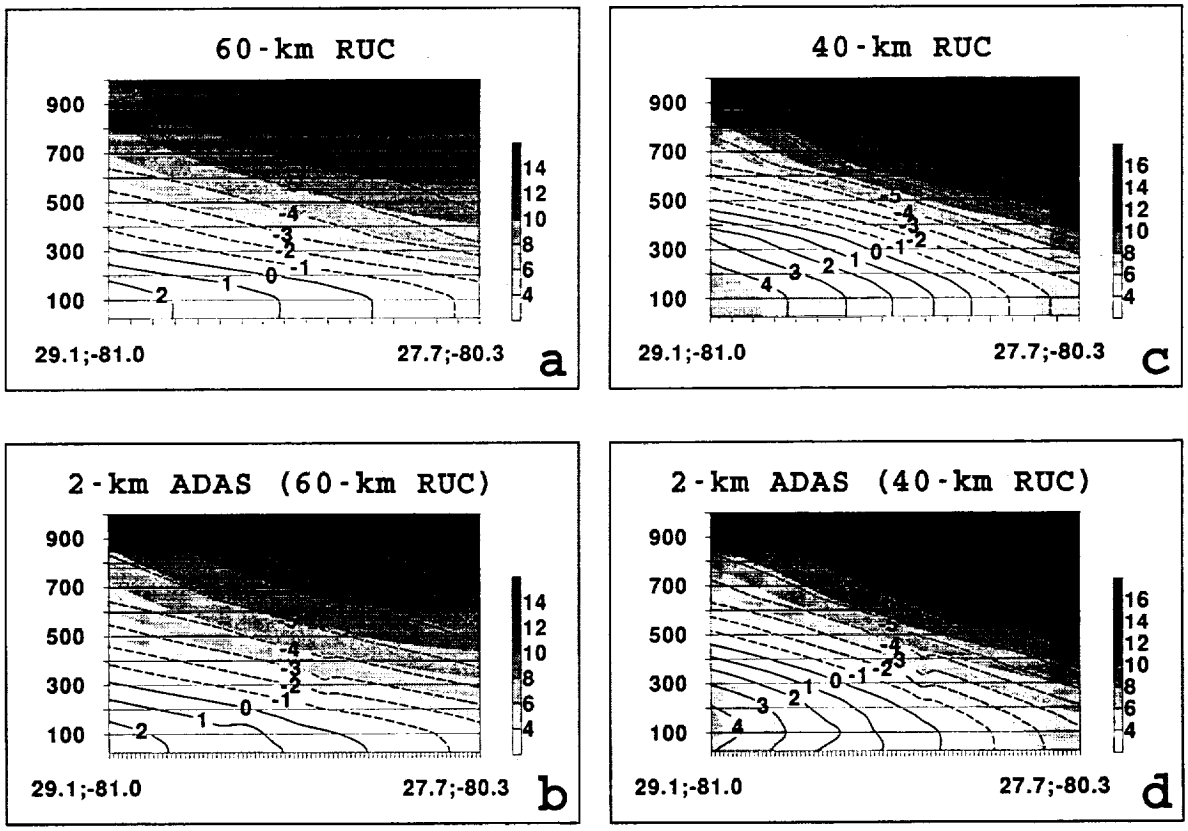

Figure 5.6. Cross sections of wind speed (m s^{-1}) and the tangential wind component along the line in Figure 5.5 at 1400 UTC 12 December for the a) 60-km RUC, b) 2-km ADAS using the 60-km RUC background, c) 40-km RUC, and d) 2-km ADAS using the 40-km RUC background. Wind speeds are shaded according to the scales provided and the tangential wind components are contoured every 1 m s^{-1}, where dashed contours denote negative tangential winds. The vertical coordinate is in meters.

According to the results in Figure 5.6, there is not much difference between the 2-km ADAS analyses and the RUC analyses in this particular case. Thus, there is limited utility in analyzing the frontal zone in the cool season case. From analysis results using the 40-km and 60-km RUC background fields, two important points can be concluded:

- The wind field is depicted more accurately by utilizing the 40-km instead of the 60-km RUC as a background field. Since the 40-km RUC model has replaced the 60-km RUC at the National Centers for Environmental Prediction, the higher resolution RUC background field will be available for possible future real-time LDIS runs.

- ADAS provides little additional detail of the wind field associated with the frontal zone compared to the 40-km RUC in this instance. However, additional case studies of Florida fronts are necessary to determine whether LDIS can provide significant added value in these weather situations.

5.3 Cloud Diagnostic Utilities

The CCS has the capability to provide valuable information to forecasters about the properties of clouds. With the proper visualization and display techniques, fast and efficient assessments of the evolution of cloud structures can be conducted to help determine cloud thickness, cloud heights, ceilings, and the potential for cloud electrification and lightning. This section presents example cloud products derived from the CCS and the potential value added in using examining the analysis products compared with the individual data sets.

5.3.1 Cloud Visualization

Since it is difficult to quantify cloud parameters, one of the objectives in this section is to portray the value of the ADAS cloud products using the appropriate visualization software. One of the software tools designed for improved visualization capabilities is the Vis-5D package. Originally developed by William Hibbard and David Santek at the University of Wisconsin Space Science and Engineering Center, Vis-5D is designed to display gridded data in three space dimensions, one time dimension, and a dimension for enumerating multiple variables (Hibbard et al. 1994). Vis-5D was selected over other visualization packages because the software is free, portable to a variety of computer workstation platforms, easy to install, and extremely user-friendly. The 3D visualization of analyses from the CCS of ADAS can provide users with a fast, qualitative assessment of the cloud coverage, depth, and type of cloud fields.

Examples of this multi-dimensional visualization are shown for both the summer and winter cases using results from the 10-km ADAS (Fig. 5.7). Isosurfaces of cloud liquid water (cloud ice) are displayed in yellow (blue) whereas the combination of both fields are depicted by a green shade. The cluster of convection in the summer case is depicted by the continuous area of cloud liquid water and cloud ice to the southwest of KSC/CCAS shown in Fig. 5.7a. The image can be tilted for perspective to interpret the depth of the cloud and distinguish between cloud liquid water and cloud ice fields (Fig. 5.7b).

In the winter case, the widespread nature of the post-frontal cloud cover is quite evident at 1400 UTC 12 December (Fig. 5.7c). In addition, the ice anvil is distinguishable from the thicker, precipitating clouds. In Figure 5.7c, the blue areas denote the cloud ice field only whereas the combination of both cloud ice and cloud liquid water shows up as green. This effect in Figure 5.7c is obtained by setting the cloud ice field to be semi-transparent on the Vis-5D display. The perspective view for the winter case shows the vertical extent of the cloud cover at the leading edge of the post-frontal convection as denoted by the deep layer of cloud liquid overlaid by cloud ice (Fig. 5.7d). In addition to the 3D structure of multiple cloud variables, Vis-5D can depict time animations of these quantities (not shown). Enhanced visualization of cloud variables in 3D combined with temporal animations can provide the user with a more complete picture of cloud fields than is possible with an examination of only satellite data.

This page intentionally left blank.

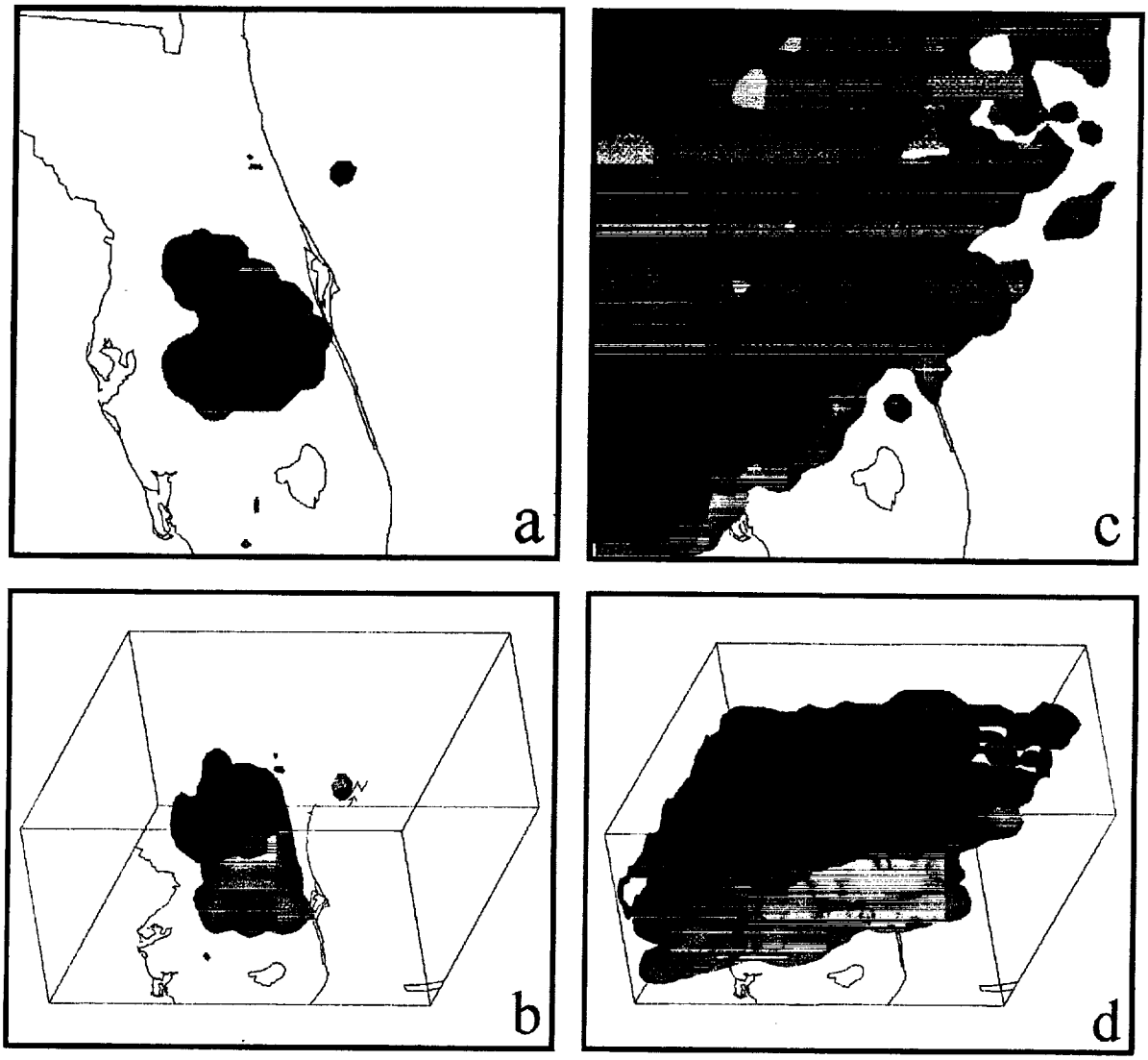

Figure 5.7. Vis-5D-generated isosurfaces of cloud liquid (q_c) and cloud ice (q_i) mixing ratios. Valid times are 2215 UTC 26 July in panels a) and b) and 1900 UTC 12 December in panels c) and d). Yellow (blue) is q_c (q_i) greater than 0.02 g kg^{-1}. Panels a) and c) display top views while panels b) and d) display tilted perspectives of the cloud analyses.

5.3.2 Impact of WSR-88D Reflectivity Data

WSR-88D reflectivity data are critical in the CCS since cloud parameters are empirically derived from threshold values of reflectivity. Also, reflectivity data provide the most continuous source for generating the 3D structure of the cloud fields. A drawback of radar data is that each beam slopes upward with distance from the radar site. At significant distances from the radar location, the lowest elevation scan can overshoot areas of low cloud cover. This problem is partly alleviated by the incorporation of hourly METAR cloud reports which provide information about the cloud base heights.

WSR-88D reflectivity data are compared to the cloud products from the 2-km ADAS analyses. Cross sections of reflectivity and cloud products are taken along the same lines in order to make these qualitative comparisons. An exact correspondence between the reflectivity and cloud images should not be expected since the CCS also uses METAR and satellite data to construct the 3D cloud fields.

For the warm season case of 26 July 1997, thunderstorms to the southwest of KSC/CCAS are examined in order to compare the analyzed cloud structure to the reflectivity images. A large cluster of reflectivity exceeding 34 dBZ lies over southern Brevard and eastern Osceola counties at 2212 UTC (Fig. 5.8a). Within this maximum of high reflectivity are embedded areas of reflectivity greater than 50 dBZ. The coverage and intensity of this reflectivity maximum decreases slightly by 2242 UTC as the convection moves northeastward (Fig. 5.8b).

Southwest–northeast oriented cross sections through these thunderstorms along the lines in Figure 5.8 reveal the structure of the derived cloud variables from the 2-km ADAS analyses and allow for comparisons between radar reflectivity and the analyzed cloud fields. Note that the reflectivity and cloud cross sections shown in Figure 5.9 are along the exact same cross section line. The reflectivity cross section at 2212 UTC shows three distinct bands of heavy precipitation below 5 km (labeled with arrows 1, 2, and 3 in Fig. 5.9a). Reflectivity > 50 dBZ exists in columns associated with cells 1 and 2 whereas cell 3 has a weaker but still distinct reflectivity maxima. The corresponding 2-km ADAS cross section of cloud parameters (Fig. 5.9b) resembles the radar cross section qualitatively with a few minor variations. The best correspondence between Figures 5.9a and b occurs in the rain water (q_r) field. The most concentrated columns of q_r coincide with the regions of highest reflectivity as depicted by the cells 1, 2, and 3 in Figures 5.9a and b. A similar correspondence is evident between the reflectivity and q_r fields in Figures 5.9c and d especially with respect to the heaviest cell shown by the arrow.

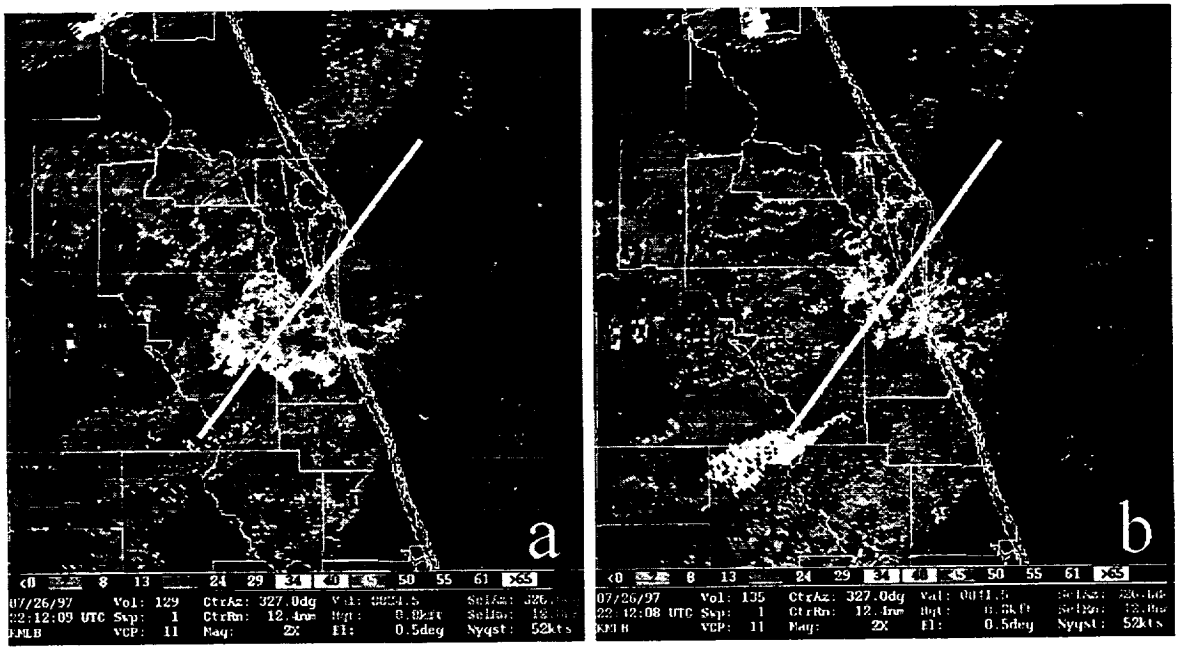

Figure 5.8. Base reflectivity images are shown from the Melbourne WSR-88D on 26 July at a) 2212 UTC and b) 2242 UTC.

The same series of radar and cloud analysis figures is displayed for the cool season case at 1700 UTC and 1900 UTC 12 December. The base reflectivity images are shown first followed by northwest–southeast cross sections of reflectivity and cloud variables. At 1700 UTC, a southwest–northeast elongated band of precipitation, with embedded areas of heavier convection, extends from northwestern Polk county through much of Volusia county (Fig. 5.10a). Isolated convection occurs ahead of this precipitation across KSC/CCAS. The main band of precipitation drifts southeastward over the next two hours and reaches the northern half of Brevard county by 1900 UTC (Fig. 5.10b). A line of heavy thunderstorms, positioned over northwestern Brevard, central Osceola, and southern Polk counties, marks the leading edge of the precipitation at this time.

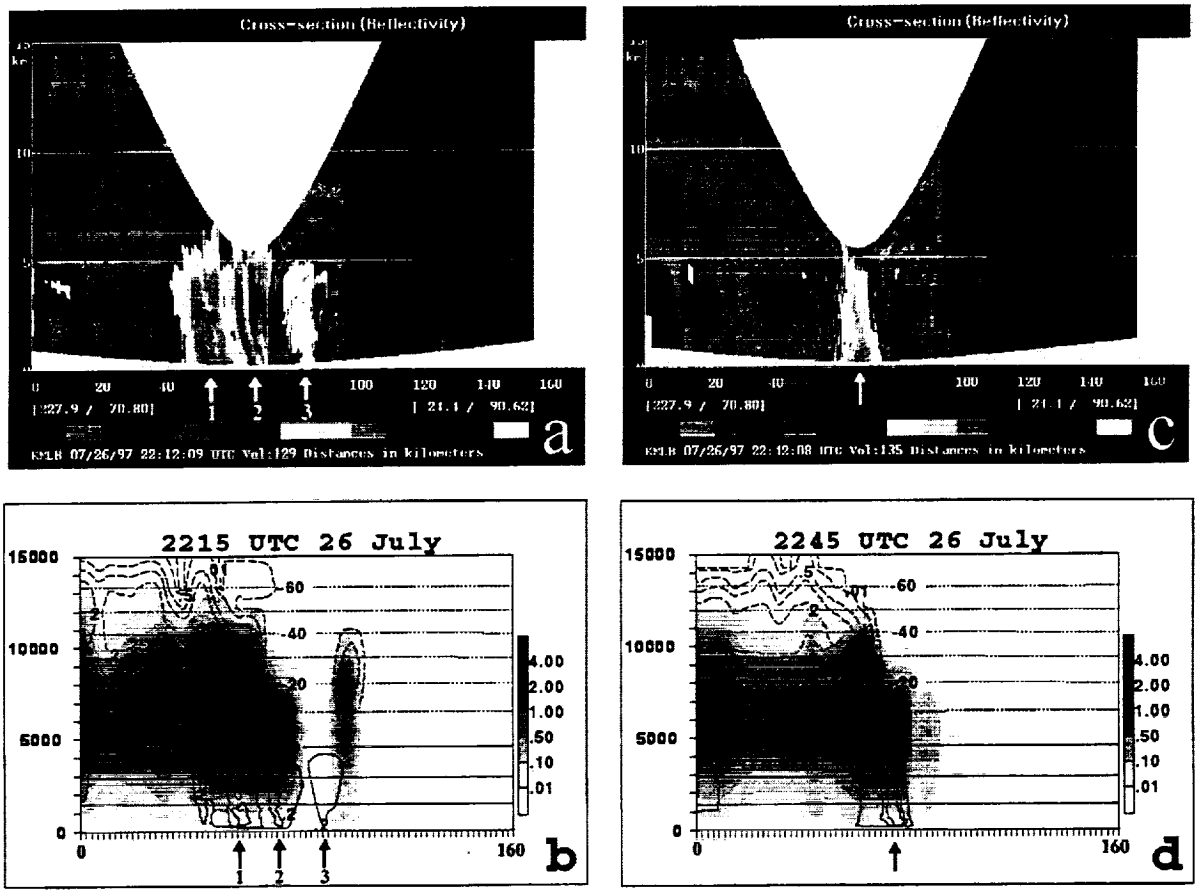

Figure 5.9. Cross sections of radar reflectivity from the Melbourne WSR-88D and 2-km ADAS analyses of cloud liquid water mixing ratio (q_c), rain water mixing ratio (q_r), and cloud ice mixing ratio (q_i). All cross sections are taken along the lines shown in Figure 5.8. Reflectivity cross sections are shown at 2212 UTC and 2242 UTC 26 July in panels a) and c), respectively, while cloud analysis cross sections are shown at 2215 UTC and 2245 26 July in panels b) and d), respectively. The vertical axes range from the surface to 15 km while the horizontal axes range from 0 to 160 km. The q_c fields (g kg^{-1}) are shaded according to the gray scale in panels b) and d). The q_r (g kg^{-1}) and q_i (g kg^{-1}) fields are shown by the solid and dashed contours, respectively, in panels b) and d). Note that isopleths for q_r (q_i) are given at 0.2, 1.0, 1.5, and 2.0 g kg^{-1} (0.01, 0.1, 0.5, 1.0, and 2.0 g kg^{-1}). Horizontal lines in panels b) and d) denote isotherms every 10 °C with negative temperatures shown by dotted lines. Individual cells are marked by arrows.

A northwest–southeast cross section through the area of precipitation at 1700 UTC reveals excellent correspondence between the radar cross section (Fig. 5.11a) and cloud products (Fig. 5.11b). The heaviest convective cell over KSC/CCAS at 1700 UTC (Fig. 5.11a) is depicted quite well in the cloud analysis cross section as noted by the concentrated column of cloud liquid water (q_c) and q_r (arrow in Figure 5.11b). The uniform area of 18–29 dBZ reflectivity at and below 7.5 km (left portion of Figure 5.11a) is denoted by the 2-km ADAS q_c and cloud ice (q_i) fields between 2.5 km and 7.5 km (Fig. 5.11b). Furthermore, somewhat of an ice anvil is seen between 9 km and 12 km with maximum q_i exceeding 1.0 g kg^{-1}. By 1900 UTC, the thickest and most concentrated q_c shifts southeastward (Fig. 5.11d) corresponding to the maximum reflectivity in Figure 5.11c. Again, the q_r field is in close agreement with the highest reflectivities as denoted by the embedded cells labeled with arrows 1 and 2 in Figures 5.11c and d.

It is interesting to note the substantial cone of silence above 5 km in the center of the warm season radar cross sections (Figs. 5.9a and c). The influence of the cone of silence is somewhat visible in the cloud analysis as the q_c fields slope downward above cells 1 and 2 (Fig. 5.9b). However, this data void is not as prevalent in the cloud analyses because the CCS interpolates data in three dimensions between radar beams and blends the data with the background. Furthermore, the incorporation of GOES-8 IR data builds cloud information at upper levels. These characteristics of the CCS lessen the impact of the cone of silence on the analyzed 3D cloud fields.

Another characteristic of radar data is the upward slope of the beams with distance from the radar site. The influence of the sloped radar beams on the cloud analysis is depicted in Figure 5.9. The lower edge of the reflectivity data extends upward from the center to the endpoints of the cross section (~1.0–1.5 km in Figs. 5.9a and c) which corresponds to the upward slope of the lowest elevation scan. This same pattern exists in the analyzed cloud variables as the lower edge of the q_c and q_r fields extends upward from the center to the left portion of the cross sections (Figs. 5.9b and d).

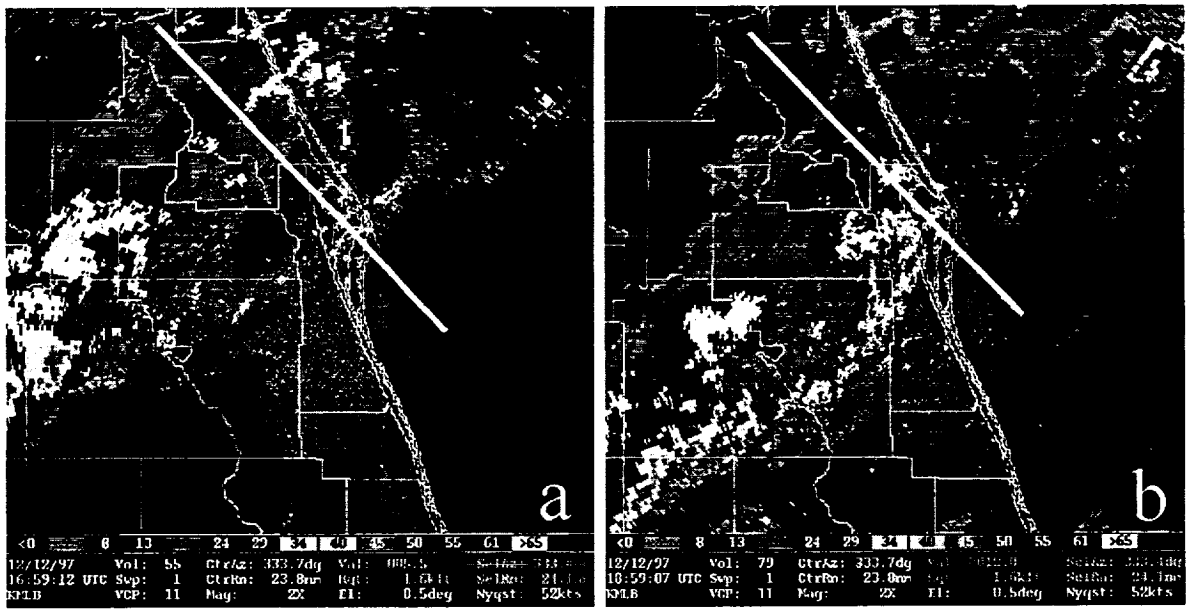

Figure 5.10. Base reflectivity images from the Melbourne WSR-88D on 12 December at a) 1659 UTC and b) 1859 UTC.

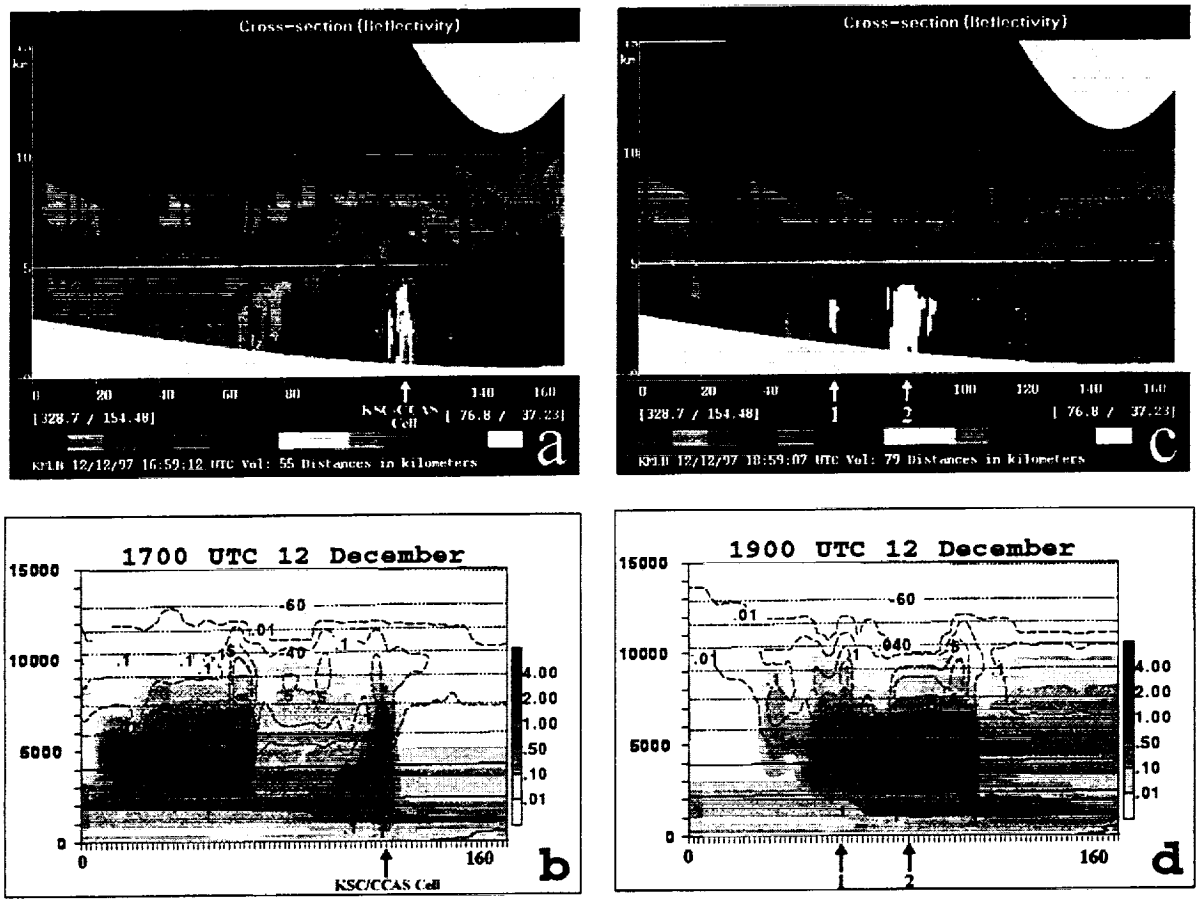

Figure 5.11. Cross sections of radar reflectivity from the Melbourne WSR-88D and 2-km ADAS analyses of cloud liquid water mixing ratio (q_c), rain water mixing ratio (q_r), and cloud ice mixing ratio (q_i). All cross sections are taken along the lines shown in Figure 5.10. Reflectivity cross sections are shown at 1659 UTC and 1859 UTC 12 December in panels a) and c), respectively, while cloud analysis cross sections are shown at 1700 UTC and 1900 12 December in panels b) and d), respectively. The vertical axes range from the surface to 15 km while the horizontal axes range from 0 to 160 km. The q_c fields (g kg^{-1}) are shaded according to the gray scale in panels b) and d). The q_r (g kg^{-1}) and q_i (g kg^{-1}) fields are shown by the solid and dashed contours, respectively, in panels b) and d). Note that isopleths for q_r (q_i) are given at 0.1, 0.5, and 1.0 g kg^{-1} (0.01, 0.1, 0.5, and 1.0 g kg^{-1}). Horizontal lines in panels b) and d) denote isotherms every 10 °C with negative temperatures shown by dotted lines. Individual convective cells are marked with arrows.

5.3.3 Impact of METAR Cloud Observations

In a typical real-time configuration, a complete cloud analysis is possible only at the top of the hour when METAR cloud reports are available in addition to satellite and WSR-88D data (see discussion in Section 3.3.2). Unfortunately, due to the limited satellite data archive for both cases (refer to Tables 3.1 and 3.2), a complete cloud analysis is generated at only five analysis times for the cool season case (1400, 1600, 1700, 1900, and 2000 UTC 12 December) and no times for the warm season case. The warm-season cloud products shown in Figures 5.9b and d represent complete cloud analyses at off-hour times. However, only the cool season cloud analyses listed above can depict the impact of all data sets in the CCS of ADAS.

In the 12 December case, features evident in the analyzed cloud cross sections include the presence of multiple horizontal layers of uniform q_c especially below 5 km (Figs. 5.11b and d). Layers of q_c on the order of 0.1–0.5 g kg^{-1} appear at 1 and 4 km on the right side of the cross section in Figure 5.11b and at 0.25 km on the left side of both cross sections in Figures 5.11b and d. These horizontal cloud layers result from the incorporation of METAR cloud observations into the cloud analysis. The CCS analyzes approximately 1-km deep horizontal layers of q_c and/or q_i within a specified cutoff radius of the METAR site. The cloud mixing ratios are empirically determined based on the extent of the cloud cover (scattered, broken, or overcast) and the height of the reported cloud base (Zhang et al. 1998). The primary advantage for using METAR observations is to analyze the clouds that cannot be measured by satellite or WSR-88D data (i.e. low- or mid-level clouds below a higher cloud deck or low-level clouds beneath the lowest WSR-88D beam).

Since the warm-season satellite data archived by the AMU were only available at 15 and 45 minutes past the hour, cloud analyses are shown at off-hour times for the warm season (Figs. 5.9b and d). Therefore, no METAR cloud observations are included in the CCS products of Figures 5.9b and d. Without the influence of cloud information from hourly METAR observations, the cloud analysis cannot analyze low-level q_c below the reflectivity data. Therefore, regions of low cloud cover (< 1 km) may not be properly analyzed at sufficiently far distances from the WSR-88D site during off-hour times. Furthermore, the effects of a tilted radar beam are prevalent in the q_c field which slopes upward from right to left between the surface and 1000 m (Figs. 5.9b and d).

6.0 Data Non-Incorporation Experiments

This section discusses the methodology for the data non-incorporation (DNI) experiments and presents results from the DNI runs for the warm and cool season cases. The DNI experiments are designed to assess the impact that specific data sources from Table 2.1 have on the subsequent analyses for the warm and cool season cases. Although DNI is applied for only two cases here, the results should help users to understand the impact of missing data on LDIS analyses. This point is especially important for LDIS running in real-time since there will be instances when data are unavailable due to equipment malfunction, transmission errors, or communication problems.

6.1 Experiment Design

The DNI experiments are designed to run ADAS in the configuration described in Section 3 and withhold selected data. Given thirteen separate data sources listed in Table 2.1, there are many possible combinations for withholding certain data types. In addition, data can be excluded at select times or during the entire analysis periods. It is not practical to run all such combinations or even anticipate when certain data types or groups of data may be missing. Therefore, the DNI experiments (Table 6.1) consider a very limited subset based on primarily data type and vertical extent. For example, METAR, buoy/ship, central Florida mesonet and KSC/CCAS tower data are withheld for DNI run #5 (NOSFC) while rawinsonde and GOES-8 soundings data are withheld for DNI run #7 (NOSND). In the event that only background fields from the RUC or another regional-scale model are available, the DNI experiment #1 (NODAT) excludes all data and provides a benchmark to compare with the full analysis of all available data. Except for NOSND, data listed in Table 6.1 are excluded by ADAS on both the 10-km and 2-km domains for each 15-minute cycle during the entire warm and cool season analysis periods (see Tables 3.1 and 3.2). Since rawinsonde and GOES-8 soundings are not analyzed on the 2-km domain, NOSND is run only on the 10-km domain.

Table 6.1. Listing of data non-incorporation (DNI) experiments.

DNI Exp. #	DNI Exp. Name	Data Excluded
1	NODAT	All
2	NOAIR	ACARS, aircraft/pilot reports, cloud/WV drift winds
3	NORAD	WSR-88D
4	NOPRO	915 MHz and 50 MHz profiler
5	NOSFC	METAR, buoy/ship, central Florida mesonet, KSC/CCAS towers
6	NOSAT	GOES-8 VIS/IR imagery
7	NOSND	Rawinsondes, GOES-8 soundings

6.2 Analysis Methodology

Each 15-minute ADAS cycle on the 10-km and 2-km domain generates ~18 megabytes (MB) of output. The large volume of output results from the horizontal and vertical distribution of many variables such as pressure, temperature, wind, moisture, etc. Since ADAS is run for 33 analysis times in the warm and cool season cases, the total amount of output per case is on the order of 594 MB (18 MB x 33 cycles). Finally the full analysis cycle is repeated seven times for the DNI experiments. Therefore, the total amount of ADAS output available for analysis of the DNI experiments is on the order 4752 MB per case (594 MB x 7 DNI runs + 594 MB x 1 run including all data).

As with the design of the DNI experiments, there are several ways to analyze and present the results given the large amount of data generated by these runs. The methodology of choice highlights how DNI impacts the analysis of features such as the outflow boundary and cold front for the warm and cool season cases, respectively. To accomplish this, spatial correlation coefficients (CCs) are computed between the full (or control) analysis and each DNI run (see Appendix B for a detailed description of CC). Spatial CCs measure the degree to which patterns are similar between two fields (Anthes 1983). Values of CCs range from –1 to 1 where

1 indicates exact agreement while 0 indicates no correspondence. (Note for CCs of −1, the patterns have the same shape and intensity but opposite sign.)

The CCs are computed for u- and v-wind components, moisture (RH*), potential temperature (θ), and pressure (p). Separate CCs for these variables are calculated at each vertical level and time for the 10-km and 2-km analyses only over the area of the 2-km domain (Fig. 3.1). As a result, this technique does not measure the impact of DNI on the 10-km analyses outside of the 2-km domain. The CCs display considerable variability as a function of variable, vertical level and time for the following reasons:

- Each data type listed in Table 2.1 does not affect every analysis variable. For example, wind profiler observations do not directly impact moisture and temperature analyses.

- Each data type listed in Table 2.1 affects analyses only at a limited number of vertical levels depending on where observations are available and the vertical correlation range (see Appendix A). For example, surface wind observations do not impact wind analyses in the middle troposphere.

- Each data type affects analyses only at times when observations are available (see Tables 3.1 and 3.2).

6.3 Interpretation of Correlation Coefficients

The CCs are useful to quantify the effect of withholding certain data types on analyses from the warm and cool season cases. In general, CCs near 0 (1) indicate that the observations have relatively more (less) impact on the resulting analyses. Figure 6.1 illustrates the physical significance of a small CC that occurs between the control analysis and the analysis from DNI experiment #3 (NORAD). The magnitude of the 480-m u-wind component at 2300 UTC 26 July on the 2-km domain from the control and NORAD runs is depicted in Figures 6.1a and b, respectively. Strong positive (westerly) u-wind components present in the control run south of KSC/CCAS are nonexistent in the NORAD experiment. The difference field (NORAD − control) clearly illustrates a significant discrepancy in the u-wind component as denoted by differences as large as 12 m s^{-1} (Fig. 6.1c). The CC for the 480-m u-wind fields in Figures 6.1a and 6.1b is 0.19. This result demonstrates that WSR-88D data have a large impact in defining the structure of the outflow boundary in the wind field at this particular time and level.

A similar comparison of the surface u-wind component at 2000 UTC 26 July is shown in Figures 6.1d-f. The control analysis displays negative (easterly) u-wind components extending ~60 km inland south of KSC/CCAS in association with the east coast sea breeze (Fig. 6.1d). Although METAR, buoy/ship, central Florida mesonet and KSC/CCAS tower data are withheld in DNI experiment #5 (NOSFC), the surface u-wind field still shows easterly u-wind components south of KSC/CCAS (Fig. 6.1e). The magnitude of the u-wind is 0.5−1 m s^{-1} less than in the control run as illustrated by the difference field (Fig. 6.1f). The CC for the surface u-wind fields in Figures 6.1d and 6.1e is 0.98. A CC of 0.98 indicates that the surface wind field patterns at 2000 UTC are quite similar and that data withheld in NOSFC have a relatively small impact on the analysis of the u-wind component.

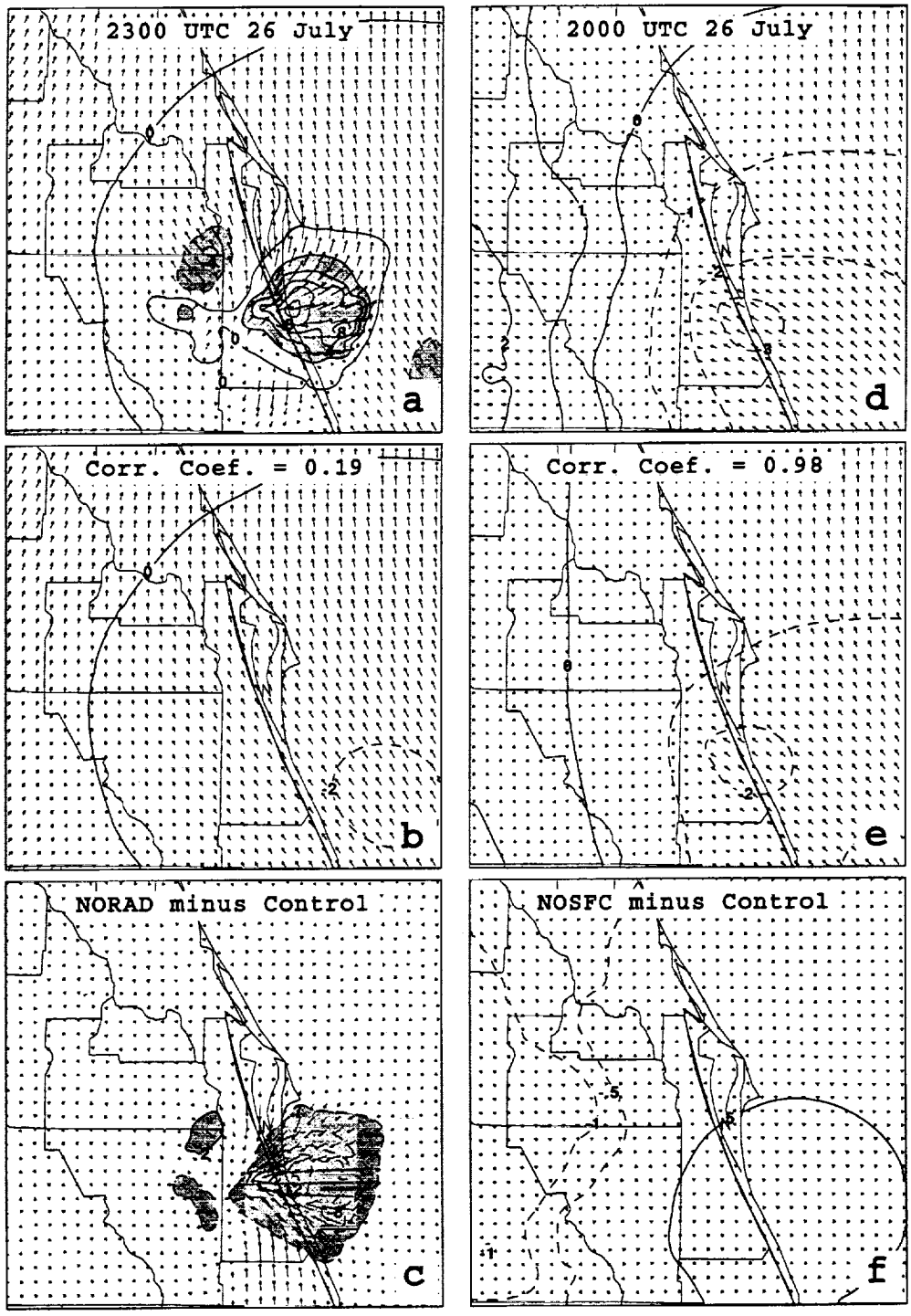

Figure 6.1. The 480-m wind vectors and u-wind component (m s^{-1}) at 2300 UTC 26 July are shown for the a) control analysis, b) data non-incorporation (DNI) experiment #3 (NORAD), and c) difference field (NORAD minus control). A similar plot of the surface wind field and u-wind component at 2000 UTC 26 July is depicted for the d) control analysis, e) DNI experiment #5 (NOSFC), and f) difference field. U-wind components > 2 m s^{-1} are shaded and negative isotachs are given by dashed lines. The spatial correlation coefficient computed between the wind fields in panels a) and b) [d) and e)] is listed in panel b) [e)].

6.4 Results of Data Non-incorporation

Given the large volume of output generated by the control and DNI runs, it is not practical to present results in the format shown in Figure 6.1. Instead, results from the DNI experiments are summarized as follows. For each warm and cool season DNI experiment, the minimum CC at any vertical level from both the 10-km and 2-km analyses is determined for a given variable and time. As stated in Section 6.2, each data type affects the analysis at a limited number of vertical levels. In fact, some observations such as cloud drift and water vapor winds can impact analyses at different levels each cycle. Therefore, the minimum CCs at any vertical level highlight the maximum impact of each DNI experiment for a specific variable and time.

The minimum CCs are then averaged over all warm and cool season analysis times when data for the DNI experiment are available in the 2-km domain as shown in Tables 3.1 and 3.2. The procedure summarizes the temporal variation in minimum CC for each variable and experiment in terms of a single number. However, time-averaging masks changes in CCs resulting from the impact that data have on the analysis at different times.

The time-averaged CCs for each variable and DNI experiment are displayed as bar charts in Figure 6.2. The following points are important for interpreting the CCs plotted in Figure 6.2:

- The absence of a DNI experiment name on any graph indicates that data from that run do not directly impact the variables listed. For example, 915 MHz and 50 MHz profiler data excluded in DNI experiment #5 (NOPRO) do not affect the analysis of moisture (RH*), potential temperature (θ), or pressure (p). Therefore, RH*, θ, and p fields from the control and NOPRO are identical and produce a CC of 1. In fact, CCs for analysis variables not affected by a given data type will be 1 at all levels and times regardless of when and where such data are available. Since these results are not useful when comparing with other CCs, the DNI experiment name is omitted from the appropriate graph.

- The absence of a bar for specific DNI experiments denotes that CCs are not computed because observations are not available for that run at any time within the 2-km domain. There are a number of time-averaged CCs equal to 1 for different variables and experiments. This result occurs when observations within the 2-km domain do not impact the analysis.

The CCs shown in Figure 6.2 provide a means for ranking the impact that data from each DNI run have on the analysis for each case. The larger (smaller) values of CC indicate that specific data have less (more) effect on the resulting analysis for a specific variable, DNI experiment, and grid. The following bullets summarize the most notable points that can be inferred from the CCs:

- WSR-88D data (NORAD) have the greatest impact on the analysis of wind (u, v) and moisture (RH*). Aircraft/cloud drift and water vapor winds (NOAIR) and profiler (NOPRO) observations have a similar effect on the wind analyses but to a much smaller extent than radar data.

- Satellite (NOSAT) and WSR-88D data (NORAD) have a more significant impact on the moisture analyses during the warm rather than cool season case. The possible reasons for this result are twofold. First, the warm season case features more fine-scale structures of localized convection that are well represented by the radar data set. Second, the cool season analyses use higher resolution 40-km RUC background grids whereas the 60-km RUC grids are used for the warm season case. In addition, the RUC background field can more appropriately resolve the large-scale features associated with a frontal zone compared to the small-scale features associated with convection.

- Surface data (NOSFC) have a much greater impact on the analysis of zonal wind (u) during the warm rather than cool season. This is likely due to the characteristics of the warm season case selected in which a strong zonal outflow boundary deviated significantly from the RUC background winds. In general, the surface data should have a more significant impact on the complete wind field in the warm rather than cool season.

- Rawinsonde and GOES-8 (NOSND) sounding data have the most significant influence on the analysis of potential temperature (θ) and pressure (p).

- There are no clear trends to indicate that specific data have more or less impact on 10-km versus 2-km analyses.

The DNI experiments suggest that WSR-88D data have the most significant impact on the wind and moisture analyses for both the warm and cool season cases. However, this result can be misleading because each case is characterized by substantial precipitation and hence the presence of targets needed to produce reflectivity and radial wind data. Although the WSR-88D has the highest spatial resolution compared with other sensors listed in Table 2.1, these data would have much less of an impact on the analyses in cases with limited or no radar targets. In order to address the limitations of using only two cases for DNI experiments, CCs could be computed from analyses over a period of several weeks. Such an effort would require substantial computing and data processing resources, but would provide a more representative sample of diverse weather scenarios to assess the relative impact of each data set on the subsequent analyses.

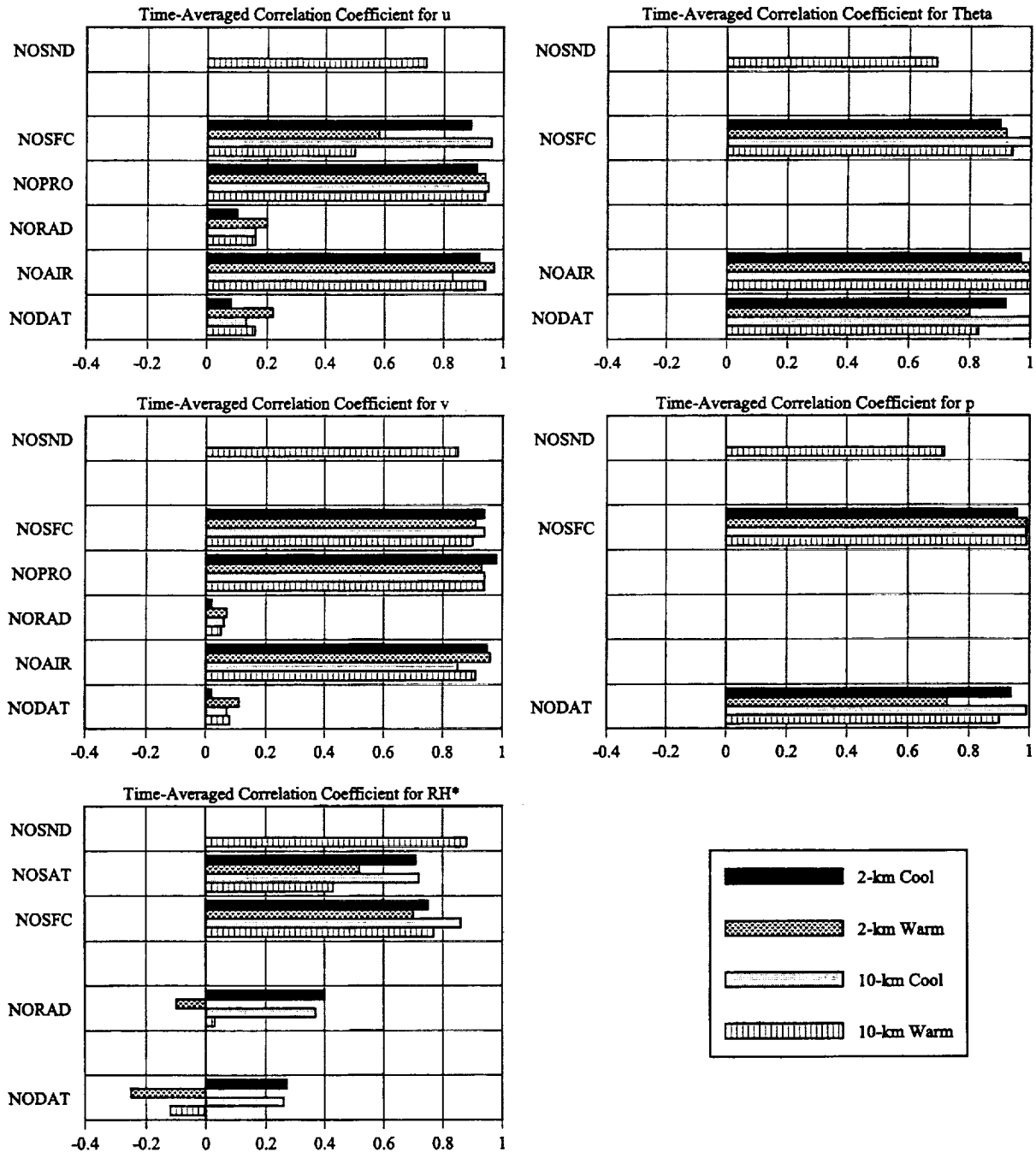

Figure 6.2. Time-averaged correlation coefficients (CCs) for data non-incorporation (DNI) experiments as a function of variable, case, and grid domain. The absence of a DNI experiment name on any graph indicates that data from that run do not directly impact the variables in question. The absence of a bar for specific DNI experiments denotes that CCs are not computed. See text for details.

7.0 Summary and Remaining Issues

This section summarizes results from the AMU task on the Local Data Integration System (LDIS) and central Florida data deficiency. The objectives of the task were to identify all existing meteorological data sources within 250 km of KSC/CCAS, identify and configure an appropriate LDIS to integrate these data, and implement a working prototype to be used for limited case studies and data non-incorporation experiments. The section concludes with a discussion of issues that need to be addressed for a real-time, operational version of LDIS.

7.1 Summary of Central Florida Data Deficiency

The utility of LDIS depends largely on the reliability and availability of both in-situ and remotely-sensed observational data. Therefore, it was important to document all existing meteorological data sources around central Florida that can be incorporated by LDIS. Results from the central Florida data deficiency portion of the task can be summarized as follows:

- Data density and coverage in east central Florida varies considerably depending on level in the atmosphere, distance from KSC/CCAS, time of day, and weather conditions.

- Rawinsondes provide the least spatial and temporal resolution of all sensors.

- Radar observations from the Melbourne WSR-88D have the best spatial resolution (between 0.2-1.0 km depending on range) but provide measurements of only reflectivity, radial velocity, and spectrum width.

- Among the measured variables in east central Florida, wind is the most represented whereas moisture is the least represented..

- The central Florida mesonet consists of existing surface meteorological and hydrological data available from the National Weather Service in Tampa and data servers at Miami and Jacksonville. However, the utility of these data for operational use is limited mainly because there are relatively few additional meteorological observations within 50 km of KSC/CCAS to supplement existing METAR and KSC/CCAS tower reports.

- With the exception of level II WSR-88D data, all other data are routinely available in real-time either locally from the 45 WS and SMG MIDDS or remotely from external sources.

- In general, the real-time data streams available for use in LDIS are currently not quality controlled (QC'ed) at the source location. Since there is no guarantee that QC will be performed prior to ingesting data into LDIS, the LDIS should have the capability to handle QC.

7.2 Summary of LDIS

The Advanced Regional Prediction System (ARPS) Data Analysis System (ADAS) was selected and configured for the prototype LDIS. For the analysis of observational data, ADAS uses an iterative successive correction method that converges to statistical or optimum interpolation. In addition, ADAS features a complex cloud scheme for moisture data assimilation and algorithms to handle the QC of data incorporated by the analysis scheme.

ADAS was configured to run with 30 vertical levels over outer and inner grids with horizontal resolutions of 10 km and 2 km, respectively. Observational data for a warm season (26-27 July 1997) and cool season case (12 December 1997) were incorporated into ADAS every 15-minutes at 0, 15, 30, and 45 minutes past the hour over a period of 8 hours for each case. With the exception of GOES-8 imagery, the data sets for each case are fairly complete and provide a reasonable representation of data that would be available to run ADAS in real-time.

Results from 10-km and 2-km analyses of winds and clouds for the case studies were presented to examine the fidelity and utility of LDIS such as ADAS. In the warm season case, the evolution of an outflow boundary was diagnosed through horizontal and vertical slices of the wind field and its associated divergence. Characteristics of a slow moving cold front and its associated cloud cover and precipitation were examined for the cool season case. Finally, a limited set of data non-incorporation (DNI) experiments was performed for the warm and cool season cases.

7.2.1 Summary of LDIS Fidelity

Fidelity was defined as the reliability of ADAS in generating features that were observed in the disparate data sets. It was important to examine fidelity in order to ensure that LDIS is capable of capturing these features when integrating many different data sources. Qualitative verifications were performed to demonstrate the fidelity of ADAS.

The trends in the ADAS wind analyses displayed a good fit to the observed trends with the exception of a few significant differences. An exact correspondence between ADAS and point observations should not be expected because ADAS integrates different types of data. In addition, variables at each grid point are determined from surrounding data and errors in the background field and observations.

Derived cloud fields from the 10-km and 2-km grids were compared to GOES-8 visible and infrared imagery. The examples from the 10-km ADAS analyses demonstrated a reasonable qualitative fit to the GOES-8 imagery; however, the 2-km cloud fields from the warm season case depicted more fine-scale details. The procedure used to remap satellite data onto the ADAS grids resulted in a slight loss of resolution on the 10-km grid whereas the 2-km grid can retain more details from the GOES-8 imagery.

Cross sections of cloud variables derived from the CCS of ADAS were compared to radar data for both case studies. It was demonstrated that the structure of the cloud analyses closely resembles the patterns in the reflectivity cross sections.

7.2.2 Summary of LDIS Utility

The utility of the LDIS is given by the value or usefulness that it can provide by integrating disparate data sets to generate analysis products that are not typically available to weather forecasters. The following points highlight the specific added value of LDIS as determined in this study:

- Sequential 15-minute wind analyses on the 2-km domain can depict the formation and propagation of a thunderstorm outflow boundary. The detailed structure of winds associated with the outflow boundary in the warm season case should be easier to visualize in real-time using ADAS rather than radial velocity data from the WSR-88D.

- Cross sections of primary and diagnostic quantities can be used to examine fine-scale spatial and temporal structures of thunderstorms that are not resolved by current national-scale operational models such as the RUC or Eta.

- The Complex Cloud Scheme (CCS) of ADAS integrates METAR, radar, and satellite data to produce a more complete picture of 3D cloud features over east central Florida compared to an examination of only satellite imagery. The CCS also derives products such as cloud ceiling, cloud tops, fractional cloud coverage, etc. at very high temporal and spatial resolutions. These high-resolution products cannot be easily obtained from the individual data sets.

- With the proper visualization and display techniques, fast and efficient assessments of the evolution of cloud structures can be conducted. The ability to simultaneously display cloud liquid water, cloud ice, rain water, and temperature analyses from the CCS can provide forecasters with information to help diagnose cloud thickness, cloud heights, ceilings, and possible cloud electrification.

- A more accurate wind structure associated with the cold front was generated when using the 40-km instead of the 60-km RUC as a background field. In general, incorporation of data in ADAS did not add much additional structure to the wind field associated with the cold front. The RUC background field can more appropriately resolve the large-scale features associated with a frontal zone for the cool season case compared to the small-scale features associated with convection for the warm season case.

7.2.3 Summary of Data Non-Incorporation

Although DNI was applied for only two cases, the results should help users to understand the impact of missing data on LDIS analyses. This point is especially important for LDIS running in real-time since there will be instances when data are unavailable. The major findings from the DNI experiments are as follows:

- WSR-88D data have the most significant impact on the wind and moisture analyses for both the warm and cool season cases. However, this result can be misleading because each case is characterized by substantial precipitation and hence the presence of targets needed to produce reflectivity and radial wind data. These data could have much less of an impact in cases with limited or no radar targets.

- Satellite and WSR-88D data have a more significant impact on the moisture analyses during the warm rather than cool season case.

- Surface data have a much greater impact on the analysis of zonal wind (u) during the warm rather than cool season because of the particular warm season case selected. In general, the surface data should have a greater impact on the complete wind field in the warm season as compared to the cool season.

- Sounding data have the most significant influence on the analysis of potential temperature and pressure.

- There are no clear trends to indicate that specific data have more or less impact on 10-km versus 2-km analyses.

7.3 Issues for Future Work with LDIS

In order to complete the current LDIS task, a prototype version of ADAS was installed and configured to run on the AMU's most powerful workstation. The analyses for the warm and cool season case incorporated archived data from all available sources including level II data from the WSR-88D. AMU work on the prototype version of ADAS revealed the following issues related to running and/or using an operational version of LDIS:

- ADAS rather than LAPS was selected for the prototype LDIS because ADAS was easier to implement and the software contains more extensive documentation. However, LAPS may be available as the operational LDIS in AWIPS for NWS MLB, SMG, and the Range Standardization and Automation for 45 WS. Therefore, future efforts with LDIS may use LAPS although both systems can be run in the prototype configuration.

- Examination of output from the prototype configuration of ADAS revealed that its utility may be limited by a lack of temporal continuity between analyses run at 15-minute intervals. Although not discussed in this report, preliminary efforts to improve temporal continuity focused on blending the previous analysis with current first guess fields. In order to optimize temporal continuity, it may be necessary to run the analysis cycle more frequently, modify the blending scheme or use a mesoscale model to provide background fields in subsequent analysis cycles.

- Several analysis cycles required more than 15 minutes of wall clock time to run both the 10-km and 2-km domains. Therefore, the prototype LDIS using ADAS in the current configuration can not be run in real time on the current workstation. For operational LDIS runs using a 15-minute analysis cycle, the configuration must be modified to execute ahead of real-time (i.e. < 15 minutes). Such modifications could include the analysis cycle frequency, and size, horizontal extent, and/or resolution of the outer and inner grids. Alternatively, LDIS could be run on a faster workstation.

- Finally, a version of LDIS should be run with available real-time data to simulate operational analysis cycles for a period of several weeks. This will provide output to assess the utility of LDIS for several different meteorological scenarios over Florida, reveal deficiencies and/or sensitivities of the real-time configuration, and provide a larger sample of cases for DNI experiments. In addition, recommendations can be made for the hardware necessary to run LDIS in an operational environment.

As mentioned in Section 1, an extension to the LDIS task was approved by consensus at the 1998 AMU T&P meeting. The bullets listed in this subsection highlight issues that will be addressed in the follow-up effort to the current LDIS task. An extension of the current task will help to reinforce the point that LDIS may provide users with a more complete and comprehensive understanding of evolving weather than can be developed by examining the disparate data sets.

8.0 References

Albers, S. C., 1995: The LAPS wind analysis. *Wea. and Forecasting*, **10**, 342-352.

Albers, S. C., J. A. McGinley, D. A. Birkenheuer, and J. R. Smart, 1996: The local analysis and prediction system (LAPS): Analysis of clouds, precipitation, and temperature. *Wea. Forecasting*, **11**, 273-287.

Anthes, R. A., 1983: Regional models of the atmosphere in middle latitudes. *Mon. Wea. Rev.*, **111**, 1306-1335.

Barnes, S. L., 1964: A technique for maximizing details in numerical weather map analysis. *J. Appl. Meteor.*, **3**, 396-409.

Benjamin, S. G., J. M. Brown, K. J. Brundage, D. Devenyi, B. E. Schwartz, T. G. Smirnova, T. L. Smith, L. L. Morone, and G. J. DiMego, 1998: The operational RUC-2. *16th Conf. on Weather Analysis and Forecasting*, Phoenix, AZ, Amer. Meteor. Soc., 249-252.

Bergthorsson, P., and B. Doos, 1955: Numerical weather map analysis. *Tellus*, **7**, 329-340.

Bratseth, A., 1986: Statistical interpolation by means of successive corrections. *Tellus*, **38A**, 439-447.

Brewster, K., 1996: Application of a Bratseth analysis scheme including Doppler radar data. Preprints, *15th Conf. on Weather Analysis and Forecasting*, Norfolk, VA, Amer. Meteor. Soc., 92-95.

Carr, F. H., J. M. Krause, and K. Brewster, 1996: Application of the Bratseth scheme to high-resolution analyses in inhomogeneous data regimes. Preprints, *15th Conf. on Weather Analysis and Forecasting*, Norfolk, VA, Amer. Meteor. Soc., 231-234.

Cole, R. E., and W. W. Wilson, 1995: ITWS gridded winds product. Preprints, *6th Conf. on Aviation Weather Systems,* Dallas, TX, Amer. Meteor. Soc., 384-388.

Daley, R., 1991: *Atmospheric Data Analysis*. Cambridge University Press, 457 pp.

Droegemeier, K. K., M. Xue, K. Brewster, Y. Liu, S. K. Park, F. H. Carr, J. Mewes, J. Zong, A. Sathye, G. Bassett, M. Zou, R. Carpenter, D. McCarthy, D. Andra, P. Janish, R. Graham, S. Sanielvici, J. Brown, B. Loftis, and K. McLain, 1996: The 1996 CAPS spring operational forecasting period: real-time storm-scale NWP, Part I: Goals and methodology. Preprints, *11th Conf. on Numerical Weather Prediction*, Norfolk, VA, Amer. Meteor. Soc., 294-296.

Huschke, R. E., 1959: *Glossary of Meteorology*. American Meteorological Society, 638 pp.

Gray, D. G., C. M. Hayden, and W. P. Menzel, 1996: Review of quantitative satellite products derived from GOES-8/9 imager and sounder instrument data. Preprints, *8th Conf. on Satellite Meteor. and Oceano.*, Atlanta, GA, Amer. Meteor. Soc., 159-163.

Hibbard, W. L., B. E. Paul, D. A. Santek, C. R. Dyer, A. L. Battaiola, M-F. Voidrot-Martinez, 1994: Interactive visualization of earth and space science computations. *Computer*, **27**, 65-72.

Lambert, W. C., and G. E. Taylor, 1998: Data quality assessment methods for the eastern range 915 MHz wind profiler network. NASA Contractor Report CR-1998-207906, Kennedy Space Center, FL, 42 pp. [Available from ENSCO, Inc., 1980 N. Atlantic Ave, Suite 230, Cocoa Beach, FL 32931].

McGinley, J. A., 1995: Opportunities for high-resolution data analysis, prediction, and product dissemination within the local weather office. Preprints, *14th Conf. on Weather Analysis and Forecasting*, Dallas, TX, Amer. Meteor. Soc., 478-485.

Mendenhall, W., D. D. Wackerly, and R. L. Sheaffer, 1990: *Mathematical Statistics with Applications*. 4th ed. Duxbury Press, 818 pp.

Menzel, P. W., and J. F. W. Purdom, 1994: Introducing GOES I: The first of a new generation of geostationary operational environmental satellites. *Bull. Amer. Meteor. Soc.*, **75**, 757-781.

Neiman, S. J., W. P. Menzel, C. M. Hayden, D. Gray, S. T. Wanzong, C. S. Veldon, and J. Daniels, 1997: Fully automated cloud-drift winds in NESDIS operations. *Bull. Amer. Meteor. Soc.*, **78**, 1121-1133.

Schumann, R. S., G. E. Taylor, F. J. Merceret, and T. L. Wilfong, 1999: Performance characteristics of the Kennedy Space Center 50-MHz Doppler radar wind profiler using median filter/first guess data reduction algorithm. *J. Atmos. Oceanic Technol.*, in press.

Schwartz, B., and S. G. Benjamin, 1995: A comparison of temperature and wind measurements from ACARS-equipped aircraft and rawinsondes. *Wea. Forecasting*, **10**, 528-544.

Stamus, and McGinley, 1997: The Local Analysis and Prediction System (LAPS): Providing weather support to the 1996 summer Olympic games. Preprints, *13th Conf. on Interactive Information Processing Systems*, Long Beach, CA, Amer. Meteor. Soc., 11-30.

Veldon, C. S., C. M. Hayden, S. J. Nieman, W. P. Menzel, S. Wanzong, and J. S. Goerss, 1997: Upper-tropospheric winds derived from geostationary satellite water vapor observations. *Bull. Amer. Meteor. Soc.*, **78**, 173-195.

Zhang, J., F. H. Carr, and K. Brewster, 1998: ADAS cloud analysis. Preprints, *12th Conf. on Numerical Weather Prediction*, Phoenix, AZ, Amer. Meteor. Soc., 185-188.

Appendix A

Objective Analysis Procedure of ADAS

This appendix introduces the successive corrections method (SCM) in Section A1 and the Bratseth objective analysis procedure in Section A2. In addition, a summary of the selectable analysis parameters is presented in Section A3. Portions of this appendix are based on Bergthorsson and Doos (1955), Bratseth (1986), Daley (1991) and Carr et al. (1996).

A1. Successive Corrections Method

The SCM is a computationally inexpensive objective analysis procedure that generates an analysis grid by applying multiple iterations or passes of observational corrections to a background field. The background field, also known as the first guess grid or 0th pass, can consist of climatology, a short-term model forecast, a blend of climatology and a model forecast, or a model analysis. The computational notation for the background field is given as:

$$F_b^0(\mathbf{r}_g) \tag{A.1},$$

where $\mathbf{r}_g$ is the spatial location of the gth grid point in three-dimensions, subscript 'b' represents the background field and superscript '0' stands for the 0th pass.

In order to compute the successive corrections, the background grid values are interpolated to the observation locations. The interpolated background values at the observation locations are given by:

$$F_b^0(\mathbf{r}_i) \tag{A.2},$$

where $\mathbf{r}_i$ is the spatial location of the ith observation in three-dimensions.

The observational increment is computed by taking the difference between the observation, $F_o(\mathbf{r}_i)$, and the interpolated background values. The formulation for the observational increment is given in Equation (A.3):

$$F_o(\mathbf{r}_i) - F_b^0(\mathbf{r}_i) \tag{A.3},$$

where subscript 'o' stands for the observational value.

From the observational increments, the first pass of the SCM is performed. The analyzed value at the gth grid point, $F_a^1(\mathbf{r}_g)$, is computed by adding a weighted-sum of observational increments to the background value at the gth grid point. The weights consist of normalized exponential functions and are inversely proportional to the distance between the grid point and the observation. Therefore, observations farther from (closer to) the grid point receive less (more) weight. The expression for the weights is given in Section A2. The analysis equation for the first pass is:

$$F_a^1(\mathbf{r}_g) = F_b^0(\mathbf{r}_g) + \sum_{i=1}^{n} W_{ig}\left[F_o(\mathbf{r}_i) - F_b^0(\mathbf{r}_i)\right] \tag{A.4}.$$

The subscript 'a' represents the analyzed grid value, n is the total number of observations within the computational influence radius of the grid point*, and W_{ig} is the normalized weight function based on the distance between the i^{th} observation and the g^{th} grid point.

Analysis Equation (A.4) is generalized for multiple passes of the SCM in Equation (A.5):

$$F_a^k(\mathbf{r}_g) = F_b^{k-1}(\mathbf{r}_g) + \sum_{i=1}^{n} W_{ig}\left[F_o(\mathbf{r}_i) - F_b^{k-1}(\mathbf{r}_i)\right] \qquad \text{(A.5)}.$$

The superscript 'k' represents the current computational pass (k^{th} pass) in Equation (A.5). All other notation is the same as discussed above. For each computational pass in the SCM, the previously analyzed values $F_a^{k-1}(\mathbf{r}_g)$ become the new background field for the current pass.

A2. Bratseth Objective Analysis Scheme

Bratseth (1986) designed an iterative SCM that converges to statistical or optimum interpolation (OI). An OI scheme is generally superior to SCM because it incorporates information about observational and background errors and data density in large matrices. However, OI schemes are computationally expensive because they require massive matrix inversions. The Bratseth scheme does not require matrix inversions, therefore it is more computationally efficient than conventional OI but still has the advantages of OI which account for data density and errors in the background and observations. The following discussion outlines the modifications to the SCM and presents the normalized weights which are implemented in the Bratseth objective analysis scheme.

A2.1. Modified Analysis Equation

The first pass in the Bratseth scheme is performed in the same manner as in the SCM. The background grid is interpolated to the observation locations and the new analysis value is computed at each grid point. The first modification to the SCM occurs after the first pass. In each successive pass, the observational increments are computed from the difference between the observation $F_o(\mathbf{r}_i)$ and the *analyzed* observation at the observation location $F_o^{k-1}(\mathbf{r}_i)$. Bilinear interpolation is no longer performed after the first pass. This modification produces a more accurate estimate of the observational increment. The Bratseth analysis equation and the expression for the analyzed observations are shown in Equations (A.6a) and (A.6b), respectively.

$$F_a^k(\mathbf{r}_g) = F_b^{k-1}(\mathbf{r}_g) + \sum_{i=1}^{n} W_{ig}\left[F_o(\mathbf{r}_i) - F_o^{k-1}(\mathbf{r}_i)\right] \qquad \text{(A.6a)}$$

$$F_o^k(\mathbf{r}_i) = F_o^{k-1}(\mathbf{r}_i) + \sum_{j=1}^{n} W'_{ij}\left[F_o(\mathbf{r}_j) - F_o^{k-1}(\mathbf{r}_j)\right] \qquad \text{(A.6b)}$$

---

*An influence radius (or cutoff radius) is often used to save on computation time. At sufficiently far distances from a grid point, the weighted observational increment has a negligible contribution toward the analyzed value. Therefore, a cutoff radius is applied beyond which the weights and observational increments are not computed.

A2.2. Bratseth Weight Functions

The other modifications to the SCM occur within the expressions for the normalized weights, W_{ig} and W_{ij}. These weights account for the distances between the grid points and the observations, the observational and background errors, and the data density in the neighborhood of observations. The characteristics of the Bratseth weight functions are presented below.

In Equation (A.6), the normalized weight applied to each observational increment is given as:

$$W_{ig} = \frac{\rho_{ig}}{\sum_{i=1}^{n} \rho_{ij} + \varepsilon^2} \qquad \text{(A.7a)},$$

with

$$\rho_{ig} = \exp\left[-\frac{(d_{ig})^2}{L^2}\right] \qquad \text{(A.7b)}.$$

ρ_{ig} is known as the correlation function and is inversely proportional to the squared distance between the g^{th} grid point and the i^{th} observation $[(d_{ig})^2]$. The correlation range (L) is determined based on the average observational spacing, the grid spacing, and the amount of local fit desired in the analyses. The value of the correlation function at a distance L from a grid point equals e^{-1}. A smaller (larger) L generates a stronger (weaker) fit to the observations. A brief discussion about the assignment of L in the 10-km and 2-km ADAS configuration is presented in Section A3.

The separate weight applied to the observational analysis equation [W_{ij} in Eq. (A.6b)] contains information about the density of the observations. The correlation function for the observational analysis equation (ρ_{ij}) is inversely proportional to the squared distance between observation locations $[(d_{ij})^2]$, given in Equation (A.8):

$$W'_{ij} = \frac{\rho_{ij} + \varepsilon^2 \delta_{ij}}{\sum_{i=1}^{n} \rho_{ij} + \varepsilon^2} \qquad \text{(A.8a)},$$

with

$$\rho_{ij} = \exp\left[-\frac{(d_{ij})^2}{L^2}\right] \qquad \text{(A.8b)}.$$

The Kronecker delta function is defined as $\delta_{ij} = \begin{cases} 1 & i = j \\ 0 & i \neq j \end{cases}$. The errors are given by $\varepsilon^2 = \frac{E_o^2}{E_b^2}$ which is the ratio of the observational error variance to background error variance. Since the weights in Equation (A.7) are inversely proportional to this error term, larger (smaller) observational errors result in smaller (larger) weights.

The relative data density around an observation is accounted for in the ρ_{ij} term [Eq. (A.7b)] used to normalize the weights W_{ig} and W_{ij}. Observations that are located in data dense areas have small distances between nearby observations (d_{ij}). A small d_{ij} corresponds to a large ρ_{ij} which leads to a large summation on the denominators of W_{ig} and W_{ij}. Therefore, observations located in data dense (sparse) regions receive less (more)

weight. Ultimately, this weighting scheme leads to a more representative analysis because the grid point values are not biased toward data rich regions as in typical SCMs.

A3. The Multi-pass Configuration of ADAS

A summary of the number of passes, the correlation ranges (L), and the data used for each pass is provided in Table A1. Separate correlation ranges are used for the horizontal and vertical scales because ADAS assumes a scale separation in the analysis grid. The influence ranges L_h and L_v are carefully chosen for each data source in order to retain observational features and to prevent data from influencing too much (or too little) of the analysis grid. Data with a fine (coarse) horizontal resolution are assigned a small (large) L_h in order to preserve the resolvable features of the data source. In addition, a small L_v is used for data with fine vertical resolution (e.g. KSC/CCAS profilers and towers) and for data that should have a limited vertical influence (e.g. METAR). An observation located at a horizontal (vertical) distance L_h (L_v) from a grid point receives a weight of e^{-1}. At larger (smaller) distances, observations receive less (more) weight.

Table A1. A list of the objective analysis parameters for ADAS consisting of the horizontal (L_h; km) and vertical correlation ranges (L_v; m) and data usage for each pass for both the 10-km and 2-km grids.

	10 km Analysis			2 km Analysis		
Pass #	**L_h (km)**	**L_v (m)**	**Data Used**	**L_h (km)**	**L_v (m)**	**Data Used**
1	150	250	Air, Swnd, Raob	30	250	Air, Swnd
2	100	20	Sfc	10	20	Tower
3	50	20	Tower	10	20	Prof
4	50	20	Ssnd, Prof	4	100	Radar
5	20	100	Radar	—	—	—

Air = ACARS + Pilot reports
Sfc = METAR + central Florida mesonet + buoy/ship
Tower = KSC/CCAS towers
Radar = WSR-88D
Prof = 915 MHz and 50 MHz KSC/CCAS profilers
Ssnd = GOES-8 satellite soundings
Raob = Rawinsondes
Swnd = GOES-8 cloud drift and water vapor winds

Appendix B

Statistical Definitions Used in the Correlation Tests

Definitions and portions of the discussion in this appendix are adapted from Huschke (1959) and Mendenhall et al. (1990). Let n represent the sample size of a random variable x. The mean or expected value of random variable x is given by:

$$\bar{x} = \frac{1}{n}\sum_{i=1}^{n} x_i \tag{B.1}$$

The sample variance measures the amount of variability that occurs in a given sample and is given by:

$$\sigma_x^2 = \frac{1}{n}\sum_{i=1}^{n}(x_i - \bar{x})^2 \tag{B.2a}$$

The standard deviation is the square root of the variance:

$$\sigma_x = \sqrt{\sigma_x^2} = \left[\frac{1}{n}\sum_{i=1}^{n}(x_i - \bar{x})^2\right]^{1/2} \tag{B.2b}$$

The covariance of two random variables is defined as:

$$COV(X,Y) = \frac{1}{n}\sum_{i=1}^{n}(x_i - \bar{x})(y_i - \bar{y}) \tag{B.3}$$

A larger (smaller) absolute value of covariance represents a greater (lesser) linear dependence between the two samples of random variables. However, it is generally difficult to employ covariance by itself because an assessment of the amount of linear dependence relies upon the scale of measurement. Therefore, the covariance is normalized by the sample standard deviations of the two random variables in order to form the linear correlation coefficient:

$$\rho = \frac{COV(X,Y)}{\sigma_x \sigma_y} \tag{B.4}$$

The correlation coefficient (CC) is defined as the mutual relationship or statistical linear dependence between two samples of random variables. The CC satisfies the inequality $-1 \le \rho \le 1$, where a CC of 1 implies a perfect correlation and a CC of 0 represents no correlation.

NOTICE

Mention of a copyrighted, trademarked or proprietary product, service, or document does not constitute endorsement thereof by the author, ENSCO, Inc., the AMU, the National Aeronautics and Space Administration, or the United States Government. Any such mention is solely for the purpose of fully informing the reader of the resources used to conduct the work reported herein.